IONOSPHERIC PERTURBATIONS AND SCHUMANN RESONANCE DATA

by

Philip H. Nelson

S.B., Massachusetts Institute of Technology

(1962)

SUBMITTED IN PARTIAL FULFILLMENT
OF THE REQUIREMENTS FOR THE
DEGREE OF DOCTOR OF
PHILOSOPHY

at the

MASSACHUSETTS INSTITUTE OF TECHNOLOGY

May, 1967

Signature of Author...
Dept. of Geology and Geophysics
May, 1967

Certified by...
Thesis Supervisor

Accepted by...
Chairman, Departmental Committee
on Graduate Students

IONOSPHERIC PERTURBATIONS AND SCHUMANN RESONANCE DATA

by Philip H. Nelson

Submitted to the Department of Geology and Geophysics on

May 12, 1967

in partial fulfillment of the requirements for the degree of

Doctor of Philosophy

The properties of the first Schumann resonance mode are examined experimentally and theoretically to determine the influence of ionospheric disturbance events upon the electromagnetic earth-ionosphere cavity.

On the experimental side, a phase-sensitive tracking system has been constructed to monitor the first mode peak frequency and Q on a continual basis. The tracking system monitored signals from a vertical antenna in eastern Massachusetts for five months during 1966-1967. Data from the tracking system show that the different classes of ionospheric events are associated with different types of frequency and Q variations which last from several hours to a few days. Strong PCA and multiple SID events are strongly correlated with frequency decreases and weakly correlated with Q decreases. Magnetic storms are strongly correlated with Q increases and weakly correlated with frequency decreases.

The 1966-67 data are supplemented with other data collected during 1961-1964. The diurnal frequency pattern underwent several changes during 1961-1967. These changes and the accompaning changes in the amplitude patterns are accounted for by shifts in the thunderstorm patterns. In addition, the peak frequency, averaged over a day, has risen from 7.8 cps in 1961 to 8.2 cps in 1967.

On the theoretical side, a study of the inverse problem was made. The results show that the short term resonance variations can be used to locate ionospheric perturbations. The transmission surface representation of the earth-ionosphere cavity is solved using a Green's function technique to obtain the cavity response to perturbed ionospheric models. An iterative procedure solves the matrix problem which relates frequency changes to changes in ionospheric parameters, showing the geographic distribution of ionospheric perturbations.

Thesis supervisor: Theodore R. Madden

Title: Professor of Geophysics

ACKNOWLEDGEMENTS

I wish to thank my advisor, Professor T.R. Madden, who continually provided insight and proposed different methods of attack on various aspects of the problem. Professor Madden's skillful influence is most apparent in the attempt to merge and extend the use of the theoretical treatment and the experimental data.

I am also indebted to Dr. Martin Balser and Mr. Charles Wagner of M.I.T.'s Lincoln Laboratory for providing data from past years. Mr. Wagner spent many hours of his spare time in introducing me to the art of thorough experimental technique while acquainting me with the equipment at the Millstone Hill field site. Mr. Wagner suggested the concept of the tracking filter as a method of monitoring the Schumann resonance.

Professor A.F. Gangi's advice and enthusiasm were quite helpful during the development of the resonance mode tracker.

We are grateful for the assistance of several groups and institutions. The M.I.T. Lincoln Laboratory continued to furnish a site and facilities for a rather prolonged experiment. The High Altitude Observatory of Boulder, Colorado furnished a unique aid with their up-to-date reports on solar-geophysical activity. Dr. Klaus Bibl's ionospheric research group at Lowell Technological Institute furnished ionosonde data. All computations were performed at the M.I.T. Computation Center. The American Chemical Society provided support for the author during his graduate years, and the Office of Naval Research (Project Nr-371-401) funded the research work.

Thanks also go to Miss Jerri Columbus who typed the manuscript.

TABLE OF CONTENTS

LIST OF FIGURES

FIGURE

FIGURE

LIST OF TABLES

TABLE

CHAPTER 1

INTRODUCTION

1.1 Introductory Remarks

Viewed from the standpoint of low-frequency electromagnetic waves, the term earth-ionosphere cavity implies the space between the surface of an electrically conductive earth and the ionosphere overhead. Add the term resonance and we have the picture of an electromagnetic excitation trapped in a cavity as sound waves are trapped in an organ pipe. The fundamental resonance mode occurs at 8 cycles per second and the higher modes (maxima in the power spectrum are referred to as modes) resonate at progressively higher frequencies.

The source of the resonance energy comes from world-wide thunderstorms, and the received amplitudes vary with time at any one point, thereby reflecting the pattern of storm activity. Besides the amplitude variations, the frequencies at which the amplitude exhibits maxima (peak frequencies) and the sharpness of the mode maxima (Q) also undergo variations which are dictated by variations in the structure of the ionosphere, as well as by the relative location of the receiver and thunderstorm source.

Ionospheric changes (severe changes are termed "storms"), linked indirectly to solar disturbances, manifest themselves in a wide variety of ways, depending upon the location and "eyes" of an observer. Most methods of observation look directly overhead, or else along a radio propagation path, sampling a limited geographical portion of the ionosphere. The cavity resonances, on the other hand, are affected by ionospheric properties over the entire earth, so that changes in cavity properties reflect ionospheric changes over an extensive portion of the earth's surface.

A number of questions arise in connection with the Schumann resonances and ionospheric perturbations. What kinds of ionospheric perturbations produce the most pronounced cavity effects, what kinds of effects do we see, and how consistent are the relationships? From our observations, can we determine the location and the height of the perturbations, even in a rough fashion? Can we go even farther, and perhaps assess the relative strength of changes in ionization? This thesis answers some of these questions, indicates how others might be answered, and produces a few new puzzles in the process.

1.2 Historical Review

The subject of the earth-ionosphere cavity is fairly new, originating in 1951 when W. O. Schumann introduced his mathematical treatment of low frequency electromagnetic waves trapped between a conducting sphere and a surrounding plasma. Hence the terms Schumann resonance and earth-ionosphere cavity resonance are used interchangeably. For a lossless cavity, theoretical results predict resonant frequencies for the nth mode of $\omega_n \approx \sqrt{n(n+1)}\,c/R$, where c is the speed of light and R the earth's radius. For n=1, this gives a first mode frequency at 10.6 cps.

In the first thorough experimental investigations, Balser and Wagner (1962) measured the vertical electric field at the earth's surface in the 6-35 cps range. Their findings showed the presence of the first five modes, the power in the spectrum peaking around 8, 14, 20, 26, and 32 cps. Their investigations also showed that both the power and the frequencies of the peak power (we will call the latter peak frequencies) undergo diurnal variations which were fairly consistent with the known variations of world-wide thunderstorm activity, thereby revealing the source of cavity excitation.

Other investigators have provided further demonstrations of the presence of the cavity modes, which in general substantiate the findings of Balser and Wagner.

Using both magnetic and electric sensors, and with various recording and analysis techniques, these experimenters have investigated a variety of effects associated with the phenomena, A good representation of these efforts is found in a collection of papers edited by Blackband (1964).

Treatments of the theoretical aspects have as their goal the explanation of the observed peak frequencies and Q's in terms of ionospheric properties. One approach, termed the characteristic frequency problem, involves a contour integral which leads to a wave-guide mode representation. Wait (1964) summarized this approach for the homogeneous case. The real cavity possesses inhomogeneities both in the latitudinal direction due to the influence of the earth's magnetic field upon propagation, and in the longitudinal direction due to day-night ionization profile differences. The mathematical difficulties imposed by the inhomogeneous nature of the cavity are more easily overcome by another approach best described as an equivalent circuit formulation. In their review article, Madden and Thompson (1965) outline this approach, which represents the properties of the cavity with circuit impedance parameters. The impedance formulation is then solved by extensive use of numerical techniques. In evaluting the impedance parameters, Madden and Thompson examine the effects of several possible distrubance perturbations upon the cavity resonances. The diurnal variations of the peak frequencies are explained by the spatial relation of thunderstorm source and receiver within the low Q resonance patterns. A bibliography more extensive than the one given here is included in their review.

The theoretical models satisfactorily explain the diurnal variations of power and peak frequency, and also account for the average observed peak frequencies and Q's. The perturbed models predict possible effects in peak frequency and Q which require data on a continual basis for experimental verification. However, with the exception of the quite striking example of resonance changes caused by a high altitude explosion (Balser & Wagner, 1963; Gendrin & Stefant, 1964), the data have not been sufficiently extensive to establish a relation between ionospheric changes and peak frequency or Q effects.

1.3 Contribution of This Thesis

An electronic tracking device which employs a phase-sensitive detection scheme has proven capable of keeping continual track of the first mode resonant frequency and Q. The chief contribution of this thesis is the recording of cavity effects associated with several types of ionospheric events. In addition, first mode data collected at various times during 1962-1964 from the same antenna at the same site has been processed. The combination of these data, Balser and Wagner's 1961 data, and the 1966-1967 tracker data makes possible the evaluation of the diurnal frequency and amplitude patterns over a period of six years.

To produce model results of the resonant mode behavior, the properties of the earth-ionosphere cavity are represented by the distributed admittance and impedance of a spherical transmission surface. This thesis draws upon the work of Madden and Thompson to obtain the relationship between the transmission surface parameters and the cavity properties. An inhomogeneous associated Legendre equation describes the electrical behavior of the transmission surface. The Green's function which solves the Legendre equation neatly illuminates some of the cavity properties. The first-order perturbation solution produces model results comparable to those of Madden and Thompson.

The inverse problem is also considered. The procedure employed assumes a network of stations around the world. Storm sources can then be located using the amplitude data. Numerical experiments indicate that peak frequency data provide a means of locating ionospheric perturbations.

1.4 Thesis Outline

Chapter 2 contains the formulation of the resonance problem in terms of a network of impedances. The Green's function approximate solution of the resulting Legendre equation is derived and examined in terms of cavity properties. Model results computed using this formulation are presented in Chapter 3. Using these results we make some estimates of the diurnal frequency and amplitude variations expected at Boston during various seasons of the year.

In Chapter 4 we turn to the experimental aspects with a brief description of the resonance mode tracking equipment. Complete equipment analysis and schematics are in Appendices A and B.

In Chapter 5 we present results from the resonance mode tracker and examine effects associated with ionospheric variations. The reader unfamiliar with ionospheric phenomena will find that Whitten and Poppoff (1965) and several authors in Physics of the Earth's Upper Atmosphere (1965) present useful and well-referenced accounts. Whenever possible comparisions to the model results of Chapter 3 are made and some inconsistencies and questions are pointed out. Seasonal and longer-term data is presented and discussed.

In Chapter 6 we consider the use of multi-station resonance data and outline the results of some numerical inversion experiments. A few concluding remarks are relegated to the end of the thesis.

CHAPTER 2

MATHEMATICAL FORMULATION OF THE SCHUMANN RESONANCE PROBLEM USING A PERTURBATION TECHNIQUE

Madden and Thompson's results demonstrate the efficacy of the "transmission surface" approach to the Schumann resonance problem. The approach is possible because the energy at these low frequencies can only propagate in the guide as a single mode, the TEM mode. In their calculations, the transmission surface is represented by a spherical shell of finite circuit elements. They then examine the network behavior using finite-difference techniques. As Madden and Thompson mention in passing, it is also possible to use a perturbation technique to examine the behavior of the transmission surface, and it is this approach which will now be developed.

2.1 Transmission Surface on a Sphere

We treat the two-dimensional transmission surface in a fashion analogous to that used for the one-dimensional transmission line. In treating the transmission line, the engineering approach is to lump its distributed properties (e.g., capacitance to ground, wire resistance) into finite circuit elements. However, the physical properties are really smeared out along the line, and we will keep this distributive picture when dealing with the properties of the transmission surface.

The distributed transmission surface leads to a second order partial differential equation for the voltage. To derive this equation we consider the geometry of Figure 2-1. The area bound by heavy lines represents a small sector of area on a spherical shell. The angles θ and ϕ are the usual polar and azimuthal angles and R is the sphere's radius. We write the equation for conservation of current flow by setting the change in current flow, i_θ and i_ϕ, along the surface equal to the source current, j_s, plus the current which leaks to ground through the admittance Y. Note that the dimensions of i_θ and i_ϕ are amps/meter while j_s is in amps/meter². The equation of continuity (refer to Fig. 2-1) is:

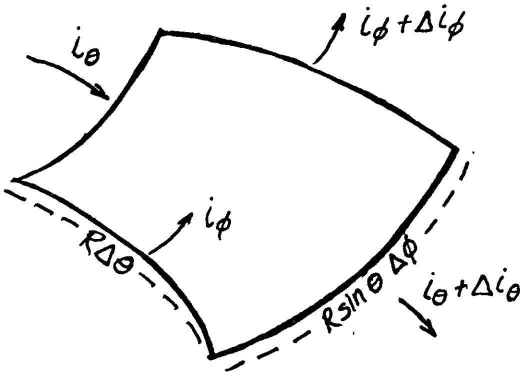

Fig. 2-1. Current flow on a spherical shell tessera.

$$\left(i_\theta + \frac{1}{R}\frac{\partial i_\theta}{\partial \theta} R\Delta\theta\right) R\sin(\theta+\Delta\theta)\ \Delta\phi - i_\theta R\sin\theta\ \Delta\phi \qquad (2\text{-}1)$$

$$+\left(i_\phi + \frac{1}{R\sin\theta}\frac{\partial i_\phi}{\partial \phi} R\sin\theta\ \Delta\phi\right) R\Delta\theta - i_\phi R\Delta\theta = \left(j_s - YV\right) R^2 \sin\theta\Delta\theta\Delta\phi$$

Since $\Delta\theta$ is small

$$\sin(\theta+\Delta\theta) \simeq \Delta\theta \cos\theta + \sin\theta$$

Substituting and reducing leaves

$$i_\theta \cos\theta + \frac{\partial i_\theta}{\partial\theta}(\sin\theta + \Delta\theta \cos\theta) + \frac{\partial i_\phi}{\partial\phi} + (j_s - YV)\, R\sin\theta$$

As $\Delta\theta \to 0$ we can ignore $\Delta\theta \cos\theta$

$$i_\theta \cos\theta + \frac{\partial i_\theta}{\partial\theta} \sin\theta + \frac{\partial i_\phi}{\partial\phi} = (j_s - YV)\, R\sin\theta \qquad (2\text{-}2)$$

We now link the voltage to the current by considering how V will change if only j_θ flows

$$\frac{1}{R}\frac{\partial V}{\partial\theta} = -i_\theta Z_\theta + i_\phi Z_{\theta\phi} \sin\theta \qquad (2\text{-}3a)$$

and if only i_ϕ flows

$$\frac{1}{R\sin\theta}\frac{\partial V}{\partial\phi} = -i_\phi Z_\phi + i_\phi Z_{\phi\theta} \qquad (2\text{-}3b)$$

Considerations by Madden and Thompson inform us that the crossterm impedances are unimportant, and that the impedances Z_θ and Z_ϕ are practically the same so we can drop the subscript on Z. Both Z and Y are functions of θ and ϕ, however. Differentiating the equations above we get:

$$-\frac{\partial i\theta}{\partial\theta} = \frac{1}{R}\frac{\partial}{\partial\theta}\left(\frac{1}{Z}\frac{\partial V}{\partial\theta}\right) = \frac{1}{RZ}\frac{\partial^2 V}{\partial\theta^2} - \frac{1}{RZ^2}\frac{\partial Z}{\partial\theta}\frac{\partial V}{\partial\theta} \tag{2-4a}$$

$$-\frac{\partial i\phi}{\partial\phi} = \frac{1}{R\sin\theta}\frac{\partial}{\partial\phi}\left(\frac{1}{Z}\frac{\partial V}{\partial\phi}\right) = \frac{1}{R\sin\theta}\left(\frac{1}{Z}\frac{\partial^2 V}{\partial\phi^2} - \frac{1}{Z^2}\frac{\partial Z}{\partial\phi}\frac{\partial V}{\partial\phi}\right) \tag{2-4b}$$

Using (2-3) and (2-4) in equation (2-2), and multiplying by -RZ/sinθ yields

$$\frac{\partial^2 V}{\partial\theta^2} + \frac{1}{\sin^2\theta}\frac{\partial^2 V}{\partial\phi^2} + \frac{\cos\theta}{\sin\theta}\frac{\partial V}{\partial\theta} - \frac{1}{Z}\frac{\partial Z}{\partial\theta}\frac{\partial V}{\partial\theta}$$

$$- \frac{1}{Z\sin^2\theta}\frac{\partial Z}{\partial\phi}\frac{\partial V}{\partial\phi} - YZR^2 V = -j_s ZR^2 \tag{2-5}$$

We now make a change of variable, X = cosθ, which gives

$$(1-X^2)\frac{\partial^2 V}{\partial X^2} - 2X\frac{\partial V}{\partial X} + \frac{1}{1-X^2}\frac{\partial^2 V}{\partial \phi^2} - \overline{YZ}R^2V = -S-T \quad (2-6)$$

where

$$S(X,\phi) = j_s ZR^2$$

$$-T(X,\phi) = \frac{1-X^2}{Z}\frac{\partial Z}{\partial X}\frac{\partial V}{\partial X} + \frac{1}{(1-X^2)Z}\frac{\partial Z}{\partial \phi}\frac{\partial V}{\partial \phi} + (YZ - \overline{YZ})\,R^2V$$

For S = T = 0, equation (2-6) resembles the equation for the surface harmonics, $Y_n^m(X,\phi)$. On the right-hand side of (2-6) are $S(X,\phi)$, the source term, and $T(X,\phi)$, the inhomogeneous term, resulting from the spatial variation of the transmission surface parameters (and eventually, of the waveguide parameters). For convenience we have placed the term $-\overline{YZ}R^2V$, involving the spatial average of YZ, on the L.H.S. and removed the difference $(YZ - \overline{YZ})R^2V$ to the R.H.S.

2.2 Perturbation Solution of the Inhomogeneous Legendre Equation

Let us now turn our attention to the mathematical problem of finding a $V(X,\phi)$ which satifies (2-6).

Define the operator

$$L \equiv \frac{\partial}{\partial x}\left((1-x^2)\frac{\partial}{\partial x}\right) + \frac{1}{1-x^2}\frac{\partial^2}{\partial \phi^2}$$

so that (2-6) takes the form

$$LV - \overline{YZ}R^2V = -S-T \qquad (2\text{-}7)$$

Employing the Green's function formulation we can write

$$V(x,\phi) = \int_0^{2\pi}\int_{-1}^{1} G(x,\phi;x',\phi')\left(S(x',\phi') + T(x',\phi')\right) dx'd\phi' \qquad (2\text{-}8)$$

The difficulty here is that T contains derivatives of V, so that we have only reposed our problem as an integrel equation. To solve (2-8) we employ a perturbation scheme. Let V^0 be the solution to

$$LV^0 - \overline{YZ}R^2V^0 = -S$$

That is,

$$V^0(x,\phi) = \iint G(x,\phi;x',\phi')\ S(x',\phi')\ dx'd\phi' \tag{2-9}$$

And let

$$-T^0(x,\phi) = \frac{1-x^2}{Z}\frac{\partial Z}{\partial X}\frac{\partial V^0}{\partial X} + \frac{1}{(1-x^2)Z}\frac{\partial Z}{\partial \phi}\frac{\partial V^0}{\partial \phi} + (YZ-\overline{YZ})R^2 V^0 \tag{2-10}$$

The first-order solution to (2-8) will be

$$V'(x,\phi) = \iint G(x,\phi,x',\phi')\ \left(S(x',\phi') + T^0(x',\phi')\right)\ dx'd\phi' \tag{2-11}$$

Proceeding in a similar fashion to higher order solutions

$$V^i(x,\phi) = \iint G(x,\phi;x',\phi')\ \left(S(x',\phi') + T^{i-1}(x',\phi')\right) dx'd\phi'$$

For our purpose the correction term T is small enough so that only the first-order solution $V^1(X,\phi)$ in (2-11) will be calculated.

2.3 Green's Function for the Two-Dimensional Legendre Equation

We now find the Green's function $G(X, \phi; X\ , \phi')$ for (2-9), which must satisfy

$$\left(L - \overline{YZ}R^2\right) G(X,\phi;X',\phi') = -\delta(X-X')\,\delta(\phi-\phi') \qquad (2\text{-}12)$$

The spherical harmonics $Y_n^m\ (X, \phi)$ must satisfy

$$\left(L + n(n+1)\right)\ Y_n^m\ (x,\phi) = 0 \qquad (2\text{-}13)$$

We expand G in terms of the Y_n^m

$$G(x,\phi;x',\phi') = \sum_{n=0}^{\infty} \sum_{m=-n}^{n} A_n^m\ Y_n^m\ (x,\phi) \qquad (2\text{-}14)$$

Substituting (2-14) into (2-12)

$$\sum_{n=o}^{\infty} \sum_{m=-n}^{n} A_n^m\ (L - YZR^2)\ Y_n^m\ (x,\phi) = -\delta(x-x')\ \delta(\phi-\phi') \qquad (2\text{-}15)$$

Substituting (2-13) into (2-15 yields

$$\sum_{n=0}^{\infty} \sum_{m=-n}^{n} A_n^m\ (n(n+1) + \overline{YZ}R^2)\ Y_n^m(x,\phi) = +\delta(x-x')\ \delta(\phi-\phi') \qquad (2\text{-}16)$$

The Y_n^m'S obey the orthogonality relations

$$Y_n^m\ (x,\phi)\ Y_k^{\ell *}\ (x,\phi)\ dxd\phi = \begin{cases} 1 & k=n\ \ \ell=m \\ 0 & \text{otherwise} \end{cases} \tag{2-17}$$

where $Y_n^{m}*$ is the complex conjugate of Y_n^m. We now multiply (2-16) by $Y_k^{1*}(X,\phi)$ and integrate over the spherical surface with respect to X and ϕ. Using the orthogonality relation (2-17) yields

$$A_k^\ell \left(\overline{YZ}R^2 + n(n+1)\right) = \iint Y_k^\ell\ (x,\phi)\ \delta(x-x')\ \delta(\phi-\phi')\ dxd\phi \tag{2-18}$$

$$= Y_k^{\ell *}\ (x',\phi')$$

Hence

$$A_k^\ell = \frac{Y_k^{\ell *}\ (x',\phi')}{n(n+1) + \overline{YZ}R^2} \tag{2-19}$$

And inserting (2-19) into (2-14) gives the expansion for G

$$G(x,\phi;x',\phi') = \sum\sum \frac{Y_n^{m*}\ (x',\phi')\ Y_n^m\ (x,\phi)}{n(n+1) + \overline{YZ}R^2} \tag{2-20}$$

Using the addition theorem of spherical harmonics (Jackson, p. 68)

(2-21)

$$P_n(\cos\gamma) = \frac{4\pi}{2n+1} \sum_{m=-n}^{n} Y_n^{m*}(x',\phi')\, Y_n^m(x,\phi)$$

where $\cos\gamma = \cos\theta \cos\theta' + \sin\theta \sin\theta' \cos(\phi-\phi')$

we can simplify (2-20) to

(2-22)

$$G(x,\phi;x',\phi') = \sum_{n=0}^{\infty} \frac{2n+1}{4\pi} \frac{P_n(\cos\gamma)}{n(n+1) + \overline{YZ}R^2}$$

2.4 Identification of Impedance Parameters with the Earth-Ionosphere Waveguide Parameters

It now remains to identify the admittance $Y(X\phi)$ and impedance $Z(X,\phi)$ with the parameters of the earth-ionosphere wave quide. Madden and Thompson carry out this operation with the result

$$Y = -i\varepsilon\omega/_h$$

$$Z = -k^2/_Y$$

where

ε = dielectric constant

ω = angular frequency

h = height of wavequide

$k = k_r + ik_i$ = propagation constant

The real and imaginary parts of the propagation constant involve the "quality factor" Q, and the phase velocity V. Q and V are related to the propagation constant by $Q = k_r/2k_i$

and

$k_r = \omega/V$

Squaring k and substituting gives

$$\begin{aligned} k^2 &= k_r^2 + 2ik_rk_i - k_i^2 \\ &= k_r^2 \left(1 - \frac{1}{4Q^2} + i\frac{1}{Q}\right) \end{aligned}$$

The impedance terms now depend upon h, V, Q, and the YZ product is:

$$YZ = -k^2 = \frac{\omega^2}{V^2} \left(1 - \frac{1}{4Q^2} + i\frac{1}{Q}\right) \tag{2-23}$$

Typical values for Q and V are computed by Madden and Thompson for various sectors of the earth where representative values of electron densities and the earth's B-field magnitude and orientation are used.

Appendix C gives h, V, and Q values for the first mode which we have used in our own calculations.

We are now in a position to examine the resonance properties of the Schumann cavity on the basis of the average properties of the individual sectors. If we substitute expression (2-23) for YZ into (2-22) we get

$$G_{\omega}(x,\phi;x',\phi') = \sum_{n=1}^{\infty} \frac{2n+1}{4\pi} \; \frac{P_n(\cos\gamma)}{n(n+1) - \frac{\omega^2}{\bar{V}^2}\left(1 - \frac{1}{4\bar{Q}^2} + i\,\frac{1}{\bar{Q}}\right) R^2} \tag{2-24}$$

The subscript ω has been added to G to emphasize the dependence of the Green's function on frequency. The bars on V and Q denote spatial averages. Keeping in mind that G_{ω} links the response at X,ϕ to the source at X',ϕ' for any frequency ω, we can see the effect which $\bar{Q}$ has on the frequency structure by examining the denominator of (2-24). If the Q were high, than we would see a strong resonance whenever n assumes integer values such that

$$n(n+1) = \frac{\omega_n^2}{\bar{V}^2} R^2$$

But $\bar{Q}$ in the earth-ionosphere cavity is low and we can see that this produces two effects. First there is an overall decrease of the resonant frequencies since they must satisfy

$$n(n+1) = \frac{\omega^2}{V} R^2 \left(1 - 1/4\bar{Q}^2\right)$$

The second effect of the high damping results from the imaginary part involving $1/\bar{Q}$. This means that at each nth resonanct frequency, the corresponding $P_n(\cos\gamma)$ which describes the spatial dependence is less dominant than it would be for high Q. Energy at frequencies above and below ω_n is correspondingly stronger. This mixing of the $P_n(\cos\gamma)$ spatial modes gives rise to a slowly changing dominant frequency as one moves away from the source, thereby explaining the diurnal frequency variations observed at any fixed receiver location. We also expect that the Green's function formulation describes the amplitude dependence of the cavity energy. Examples of the frequency and amplitude patterns are given in the next section.

CHAPTER 3

MODEL RESULTS USING THE PERTURBATION TECHNIQUE

We are now interested in obtaining a world map of the amplitude and peak frequency variations for the first resonance mode. The computational methods used to obtain the maps are first briefly described, then several examples will illustrate pertinent features and some short-term effects. Seasonal effects are predicted by combing the apparent frequency maps with world thunderstorm distribution.

We wish to caution the reader about the dual usage of the word "perturbations": the term "pertubation technique" or "perturbation solution" refers to the mathematical method used to solve the integral equation formulation of the Schumann problem; the term "perturbation model" refers to a model incorporating ionospheric parameters which differ from the standard day-night model.

3.1 Computational Procedure

The technique employed is based upon equation 2-10, derived in the last section and repeated here:

$$V'(x,\phi) = \int_0^{2\pi} \int_{-1}^{1} G\,(x,\phi;\, x',\phi') \left[S(x',\phi') + T(x',\phi')\right] dx'd\phi' \qquad (2\text{-}10)$$

Since discrete techniques are employed, we change (2-10) to subscripted notation:

$$V'(x,i\phi) = \sum_{j\phi} \sum_{jx} G_{\ell,m,n} \left[S_{jx,j\phi} + T^{o}_{jx,j\phi}\right] \Delta A_{jx,j\phi} \quad (3\text{-}1)$$

The source S and apparent sources T^o are designated by their ($jx,j\phi$) coordinates, and the Green's function G can be described by three indices (ℓ,m,n) which must depend upon the relative location of source and response ($ix,i\phi,jx,j\phi$). The surface areas at each $jx,j\phi$, location are designated A. We recall that the x suffix refers to the longitudinal direction, the ϕ suffix to the colatitude.

The model computations were carried out on a digital computer. In our computations the earth is divided into tesserae of 10° latitude by 20° longitude, so that both the x-and ϕ-suffixed indices run from 1 to 18. Inputs to the program are the frequency ϕ, the effective height of the waveguide $h(ix,i\phi)$, the $Q(ix,i\phi)$, and the phase velocity $v(ix,i\phi)$ in each sector. The Green's function G is computed for the arc distance from tesserae centers, employing a modification of equation 2-22.

Once the Green's functions $G\ell,m,n$, are known, the xeroeth-order amplitude solution $V^{o}(ix,i\phi)$ is computed by:

$$V^{o}_{ix,i\phi} = \sum_{jx=1}^{N} \sum_{j\phi=1}^{N} G_{\ell mn} S_{jx,j\phi} \tag{3-2}$$

For the standard models described below, the source was located in 2 tesserae, so that N=2. With $V^{o}(ix,i\phi)$, we can calculate the first corrective term which accounts for the inhomogeneities in the waveguide cavity. Modifying expression (2-10):

$$-T^{o} = \frac{(1-x^2)}{Z}\frac{\Delta Z}{\Delta X}\frac{\Delta V^{o}}{\Delta X} + \frac{1}{(1-x^2)}\frac{1}{Z}\frac{\Delta Z}{\Delta\phi}\frac{\Delta V^{o}}{\Delta\phi} + (YZ - \overline{YZ})\,R^2V^{o} \tag{3-3}$$

Except for R, the earth's radius, all symbols in equation (3-3) possess jx, jϕ subscripts which were omitted because of lack of space. The quantities denoted by Δ were computed by taking differences between quantities in tesserae adjacent to the jx, jϕ position, The Y's and Z's in equation 3-3 are derived from the inputs h, Q, and v, as indicated in section 2.4.

We now add the effect of all inhomogenous terms to the zeroeth-order solution to get:

$$V'_{ix,i\phi} = V^{o}_{ix,i\phi} + \sum_{jx=1}^{18} \sum_{j\phi=1}^{18} G_{mn} \, T^{o}_{jx,j\phi} \, \Delta A_{jx,j\phi} \tag{3-4}$$

The $V^{1}_{ix,\ i\phi}$, solutions must be computed for several neighboring frequencies (the angular frequency ω is incorporated in G) to derive a peak frequency pattern over the earth. In our models we compute V' at 7.5, 8.0 and 8.5 cycles per second, then fit the corresponding V's to a parabola to determine the center frequency and maximum amplitude in each tessarae. In addition, an apparent Q was found for each tesserae, based on the shape of the parabolic fit.

3.2 Model Results

The ionospheric parameters used for the h, Q, and v, inputs are those of the D11-N12 ionospheric model of Madden and Thompson. Appendix C contains the h, Q, and v, data. The source spectrum is weighted slightly towards the low end in a ratio 3.16:3.04:2.92 for the frequencies 7.5, 9.0, 8.5 cps in accordance with the results of Raemer (1961).

The models computed using the perturbation technique and presented here have been compared with Madden and Thompson's models obtained using the network solution. The D11-N12 models are in good agreement, the perturbation solution producing peak frequency trends similar to, and within 0.1 cps of, the network solution. The heavily perturbed "SID" models agree on the overall depression of peak frequency, but the perturbation solution produces a model with a pattern somewhat less diagnostic than that of the network solution. The cause of this inconsistency has not been determined. See Appendix D for further evaluation of the perturbation technique. We proceed to discuss the models obtained using the perturbation techniques in the following paragraphs.

Figure 3-1 displays the V' patterns for 7 cps and 8 cps. Since the models are symmetric about the equator we can compare the southern and northern hemispheres. It is clear that the 8 cps excitation lies closer to the first Schumann resonance, since the 7 cps amplitudes are never greater than the 8 cps amplitudes.

The V' amplitudes at three frequencies are used to determine the maximum amplitudes (Fig. 3-2), the Q's (Figure 3-2), and the peak frequencies (Fig. 3-3) in each tesserae. Since the sources are symmetrical at the equator, only one hemisphere is presented. On the peak frequency map we see basin-like contours about the source

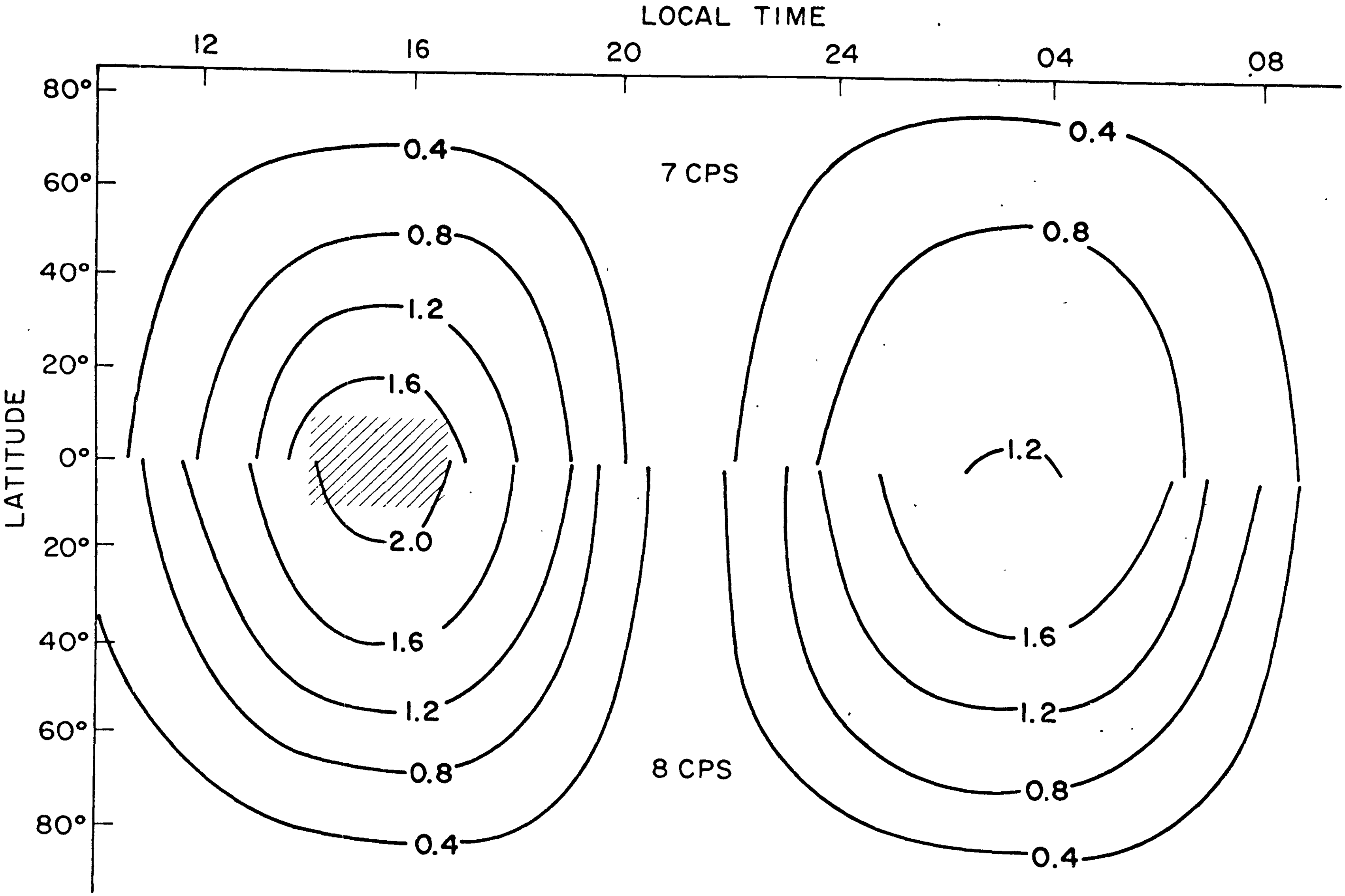

Fig. 3-1. Comparison of V^1 amplitudes over the earth's surface for the standard D11-N12 ionosphere computed for 7 and 8 cps. Hatched area designates the source area.

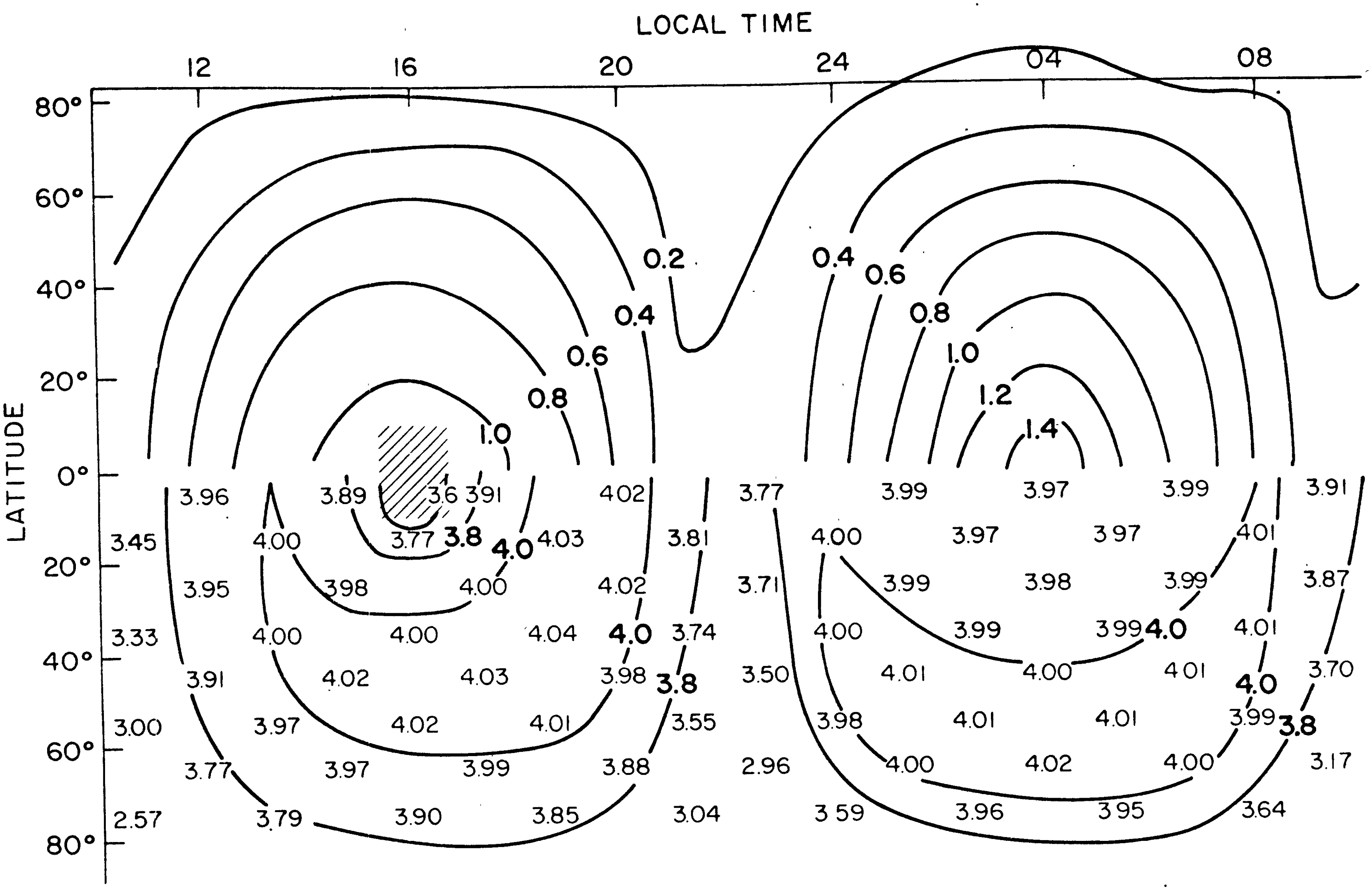

Fig. 3-2. Map of maximum amplitudes (upper half) and apparent Q (lower half) of the first Schumann mode. Source at 1600 hours within hatched area. Patterns are symmetric about the equator.

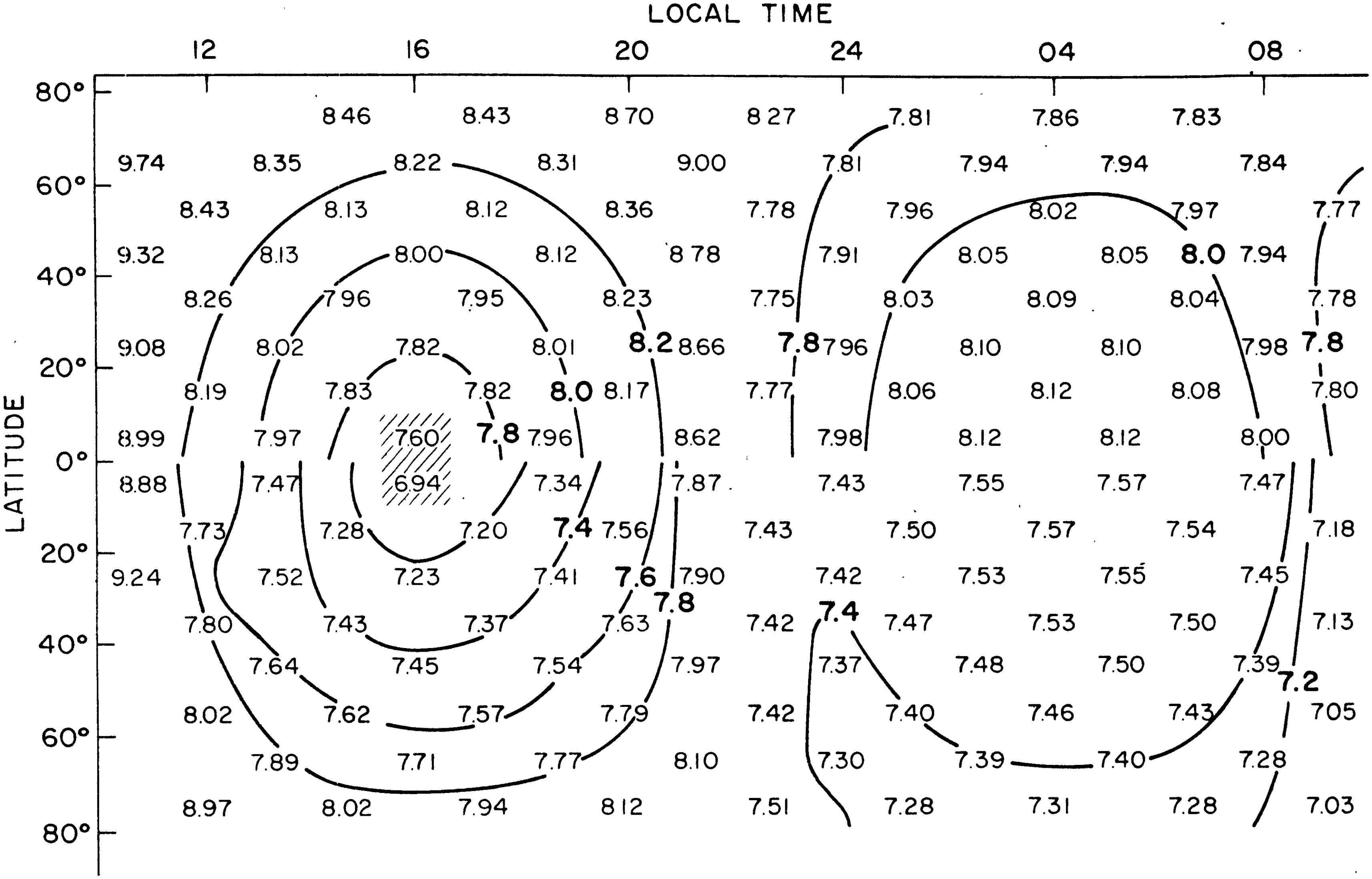

Fig. 3-3. Map of peak frequencies for standard ionospheric model (upper half) and for a perturbed "SID" ionosphere (lower half). Both patterns are symmetric about the equator.

and dome-like contours about the point antipodal to the source. At the intersection of the basin and dome frequency contours approximately 90° form the source, the frequencies become indeterminate as the amplitudes and Q's decrease (null zone). Overall, however, the Q's are fairly uniform so that no information on source-receiver relationships could be obtained from Q observations. Q information is valuable, of course, in determining whether or not a resonance peak is present.

3.3 Ionospheric Perturbations Model

Short-term changes in the lower ionosphere produce effects upon the observed frequencies of the Schumann resonances. We model these changes by perturbing the input parameters V, Q, and h. The results of a quite large theoretical "SID" event are compared to the standard frequency results in Figure 3-3. For this SID model the V's were decreased 20% and the Q's decreased 50% on the daylight side. Theprincipal effect on the peak frequencies is an overall decrease. The offset of the perturbation with respect to the source skews the frequency pattern somewhat.

3.4 Source Effects

It is evident that the source-receiver relation is the most important factor influencing the observed peak frequency. This is demonstrated in Figure 3-4 where a fifth source area is introduced at 45°N latitude. Producing only 20% of the energy in the model, the added source makes its greatest influence in what was the null zone of the lower half of the figure. It is clear that source effects must be taken care of before attempting to explain frequency observations by ionospheric changes.

3.5 Seasonal Effects

Due to the seasonal shifts of thunderstorm activity, we expect the diurnal amplitude and frequency patterns to vary throughout the year. In Figures 3-5 and 3-6 we obtain the amplitude and frequency patterns expected in eastern Massachusetts for the thunderstorm patterns in March (Handbook of Geophysics, 1960). In these figures the outside contour of the storm areas represent 10 days of thunderstorm activity per month; subsequent contours represent increments of five. Since the source-receiver relation is reciprocal, we plot the storm areas on the map of maximum amplitudes taken from figure 3-2, placing the source of the amplitude patterns at eastern Massachusetts. We now make a crude estimate of a "typical" amplitude response which might be observed in eastern

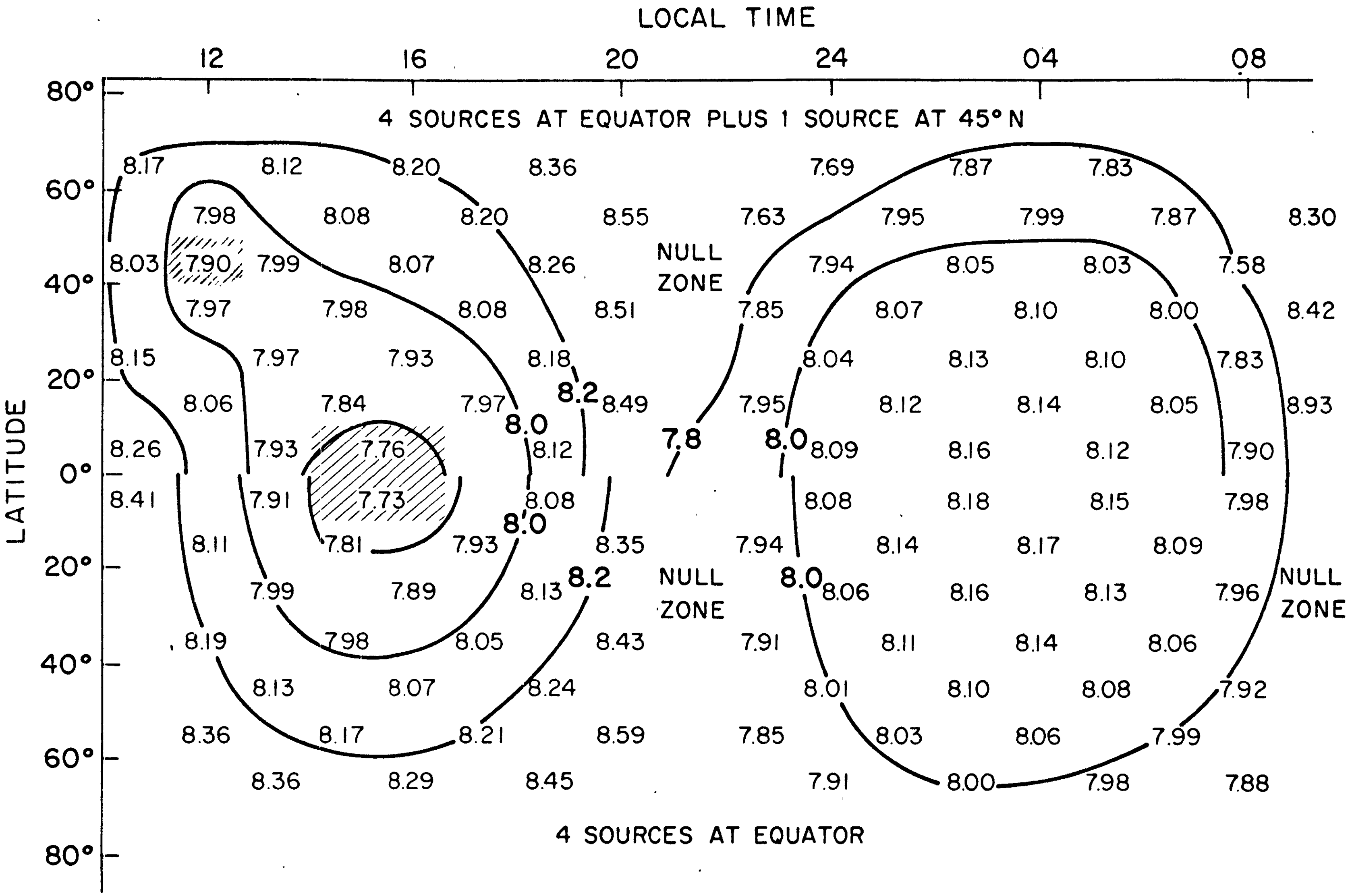

Fig. 3-4. Effect of additional source at 45°N, 1200 local time upon apparent resonant frequencies. Upper half of figure for northern hemisphere only, lower figure symmetric about equator.

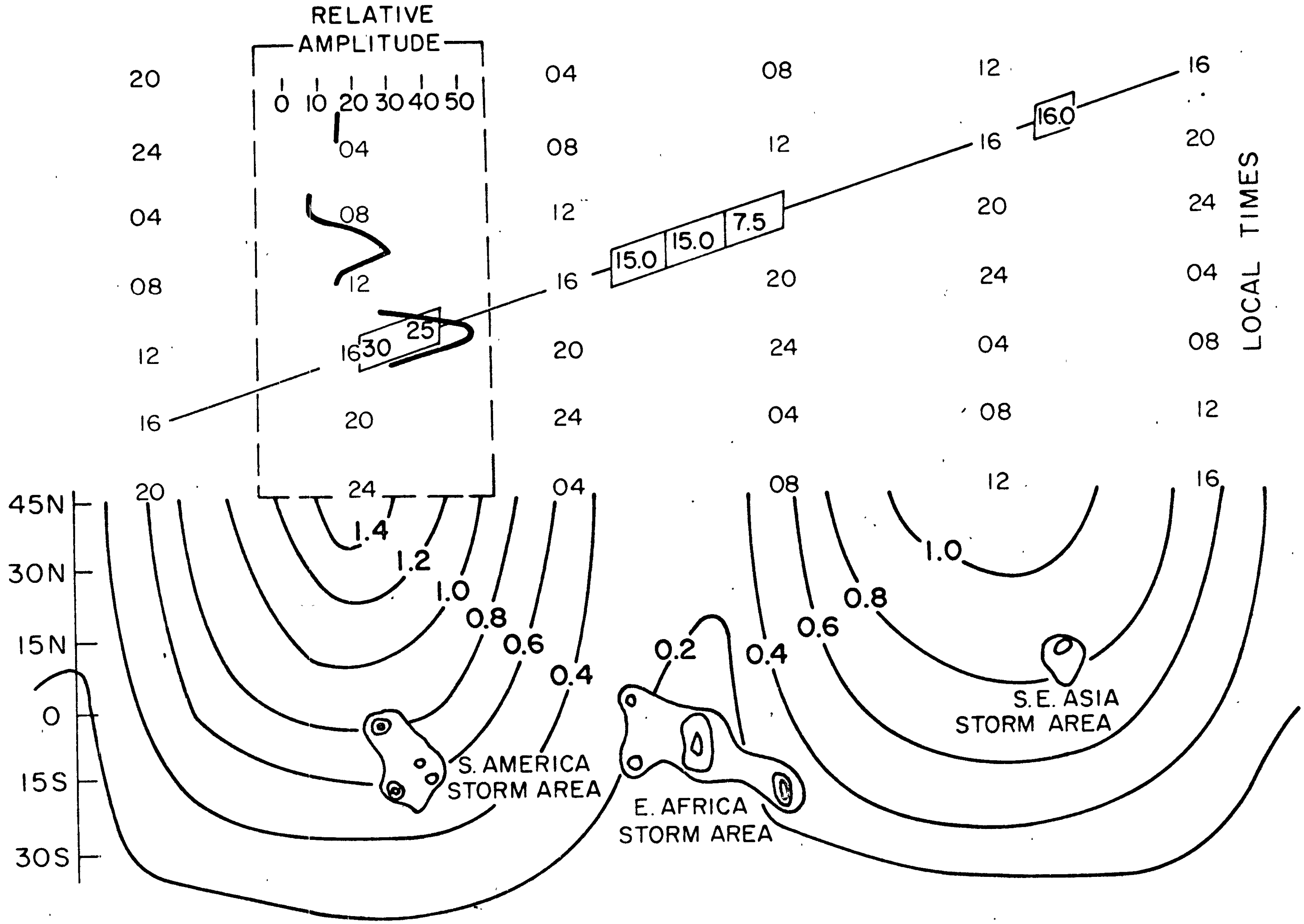

Fig. 3-5. Estimated amplitude variations at Boston for December storm patterns. The amplitudes (arbitrary scale) are proportional to storm areas and to cavity amplitude patterns, and are plotted for local time at Boston (dashed rectangle).

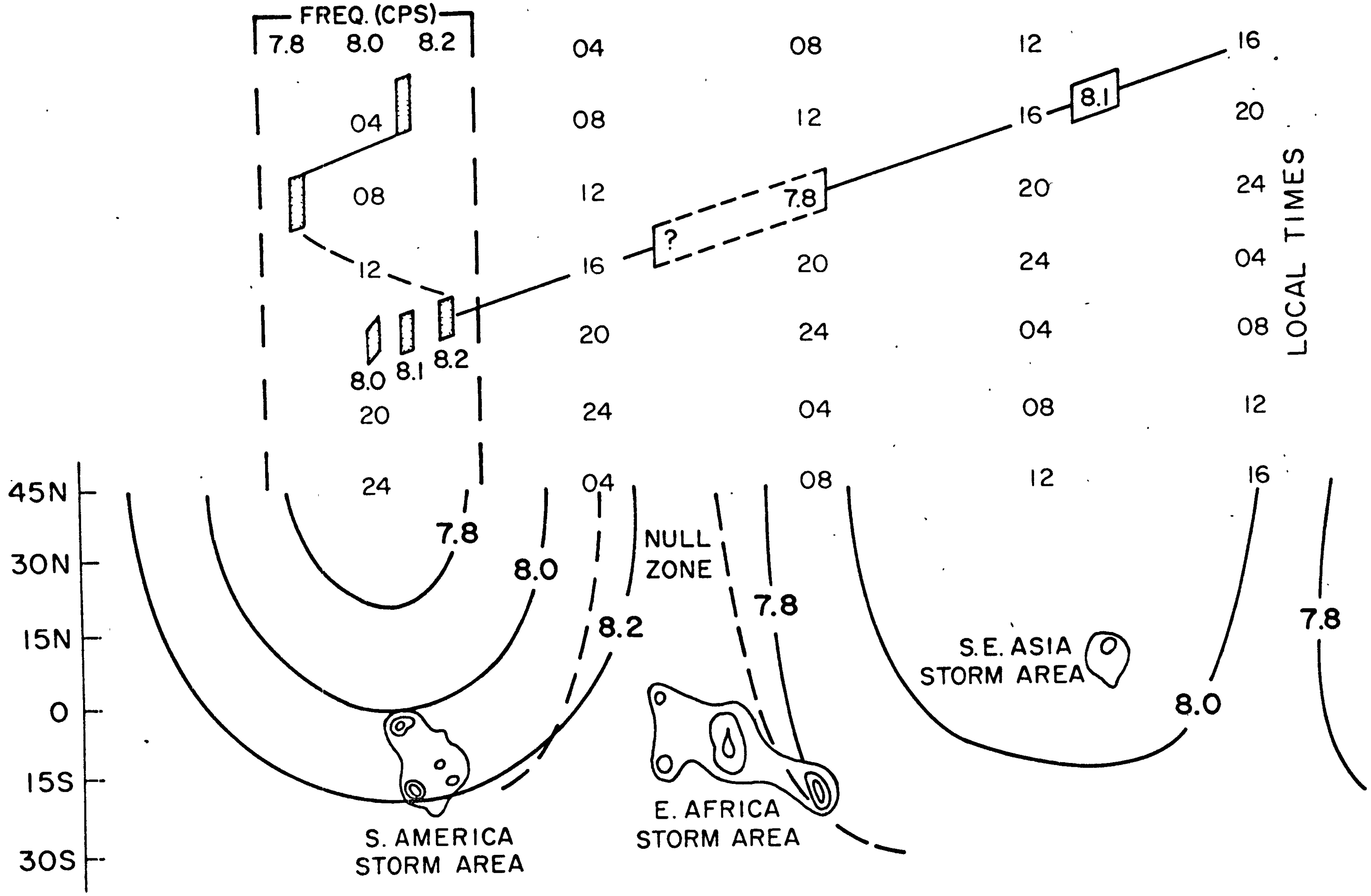

Fig. 3-6. Expected frequency changes at Boston for December thunderstorm distribution.

Massachusetts by assuming the storms occur approximately at 1600 hours local time. The numbers on the 1600 hour line on the upper part of Figure 3-5 are obtained by multiplying the area of storm centers times their position in the amplitude pattern. These numbers are then translated to the vertical axis of local time in eastern Massachusetts and plotted there. A similar procedure is carried out for the frequencies in Figure 3-6 except the source areas can not be weighted.

Plots of amplitude and peak frequency expected in eastern Massachusetts are given in Figure 3-7 for March, June, September, and December storm patterns. A source may be represented on the amplitude plot but not on the frequency plot if it lies in the null area mentioned earlier.

The graphs are only rough esitmates and are subject to the following criticisms:

1) The actual times of storm occurrence are scattered around 1600 hours and this will extend the received patterns to earlier and later times.

2) The storm statistics will not represent area or intensity on any single day.

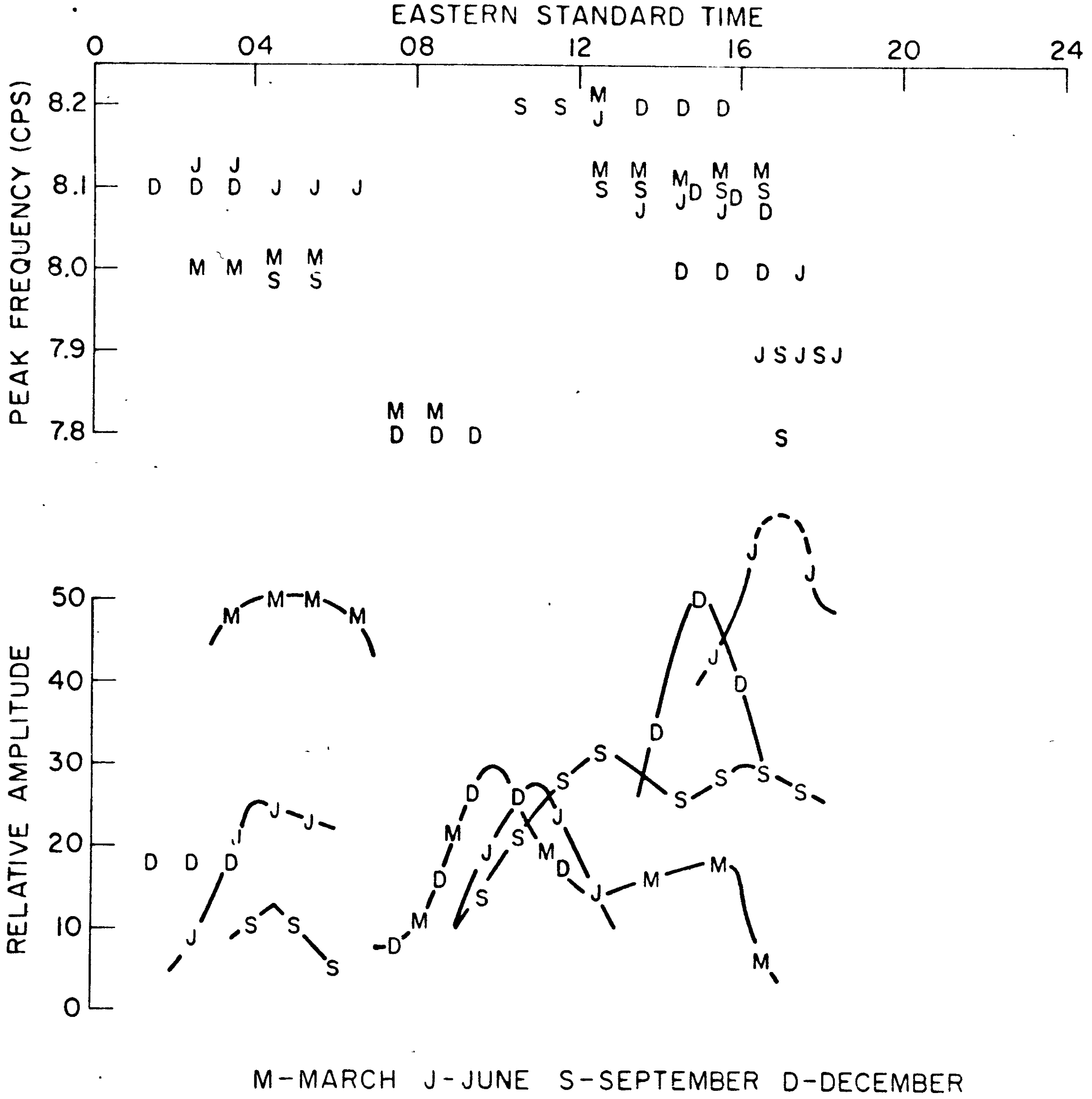

Fig. 3-7. Predicted diurnal frequency and amplitude variations of the first resonance mode, as received in eastern Massachusetts.

CHAPTER 4

A RESONANCE MODE TRACKER FOR THE FIRST CAVITY MODE

Thorough experimental investigation of the Schumann resonances requires frequency, Q, and amplitude data, obtained continuously if possible, so that short-term disturbances, diurnal, seasonal, and even annual effects can be examined. Thus far, three techniques of recording and analysis to obtain power spectra have been employed successfully by various investigators.

a) Magnetic recording and digital analysis. This is the method used by Balser and Wagner (1962a, 1962b) and also by Rycroft (1965).

b) Magnetic recording and analog analysis. Gendrin and Stefant (1964) recorded on magnetic tape and performed sonogram analysis using high-speed playback.

c) Analog filtering. In their later work Balser and Wagner (1964) constructed a bank of narrow-band filters spanning the first cavity mode and monitoring the amplitude levels at intervals up to 21 cps. A good deal of data was obtained from this system, and we are fortunate to have the use of it for our own work.

Methods a) and b) above, while successful and quite accurate, involve too much labor for long-term studies. Method c) was better suited to long-term recording but still required some further, somewhat subjective, data reduction to pick the peak frequency. This chapter describes instrumentation which tracks the peak frequency and estimates the Q rather than performing spectral analysis.

4.1 The Tracking Filter

The resonance mode tracker employs a tracking filter with variable capacitance. See Fig. 4-1 for an outline of the tracking filter. A complete block diagram is given in Fig. 4-4, circuit analysis is in Appendix A, and detailed circuitry is in Appendix B.

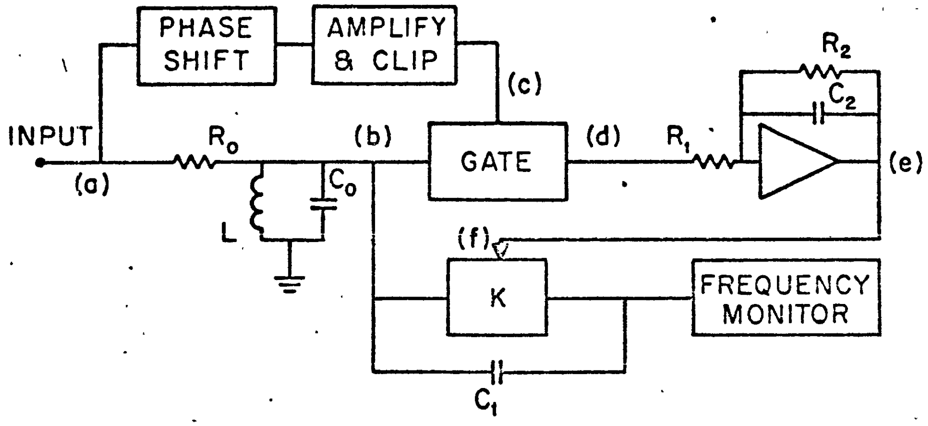

Fig. 4-1. Conceptual schematic of frequency tracking loop of the resonance mode tracker. Element K is a voltage-controlled amplifier.

It should be mentioned that the self-tracking filter bears some family resemblence to phase-lock automatic frequency contol (AFC) devices which track, in the presence of noise, a regular sinusoidal signal whose frequency is slowly varying (Gardner, 1966). In AFC circuitry a voltage controlled oscillator (VCO) controls the mixing element, or gate, through which the incoming signal passes. The output of the gate, after shaping, controls the VCO frequency and drives it to follow the incoming signal frequency. Thus, monitoring the VCO signal actually monitors the unknown frequency. For the Schumann resonances, however, we are concerned with a noise signal; instead of internal oscillator control we have used the filter concept in Fig. 4-1.

The tracking band-pass filter of Fig. 4-1 consists of Ro, L, and Co, along with capacitor C_1 which has the effect of being in parallel with Co. Amplifier K controls the effective size of C_1 and hence tunes the band-pass filter. The signal at point (d) is the result of comparing the input signal after 90^0 phase shift [path (a) - (c)] against the input signal after it has passed the tracking filter [path (a) - (b)]. The signal at point (d) is then integrated at (e) to control amplifier K. The next paragraph describes the phase-shift control in detail.

Consider a sine-wave input of frequency f. If f is the same as the center frequency fo of the band-pass filter then no phase-shifting occurs, the signals at points (b) and (c) are 90^o out of phase, and we have the sequence depicted in Figure 4-2A. Now suppose the input frequency f is greater than f_o. Then the filter appears as a capacitive reactance of angle ϕ and the signal at (b) leads the signal at (a) by $90^o - \phi$(See Fig. 4-2B). When time-averaged, the asymmmetry of the gated signal at (d) results in a negative D.C. contribution at (e). The signal at (e), when converted to a gain at (f), tunes the filter until its center frequency f_o matches f. The circuit is then back at equilibrium, as in Figure 2A, and the signal at (e) has decreased to zero. In practice, some error signal at (e) will always be needed to maintain the required gain, but if the loop gain between (d) and (f) is great enough, this error signal will be negligible. The same arguments apply if f is initially less then f_o, except now the voltage at (e) will be positive and the gain will be negative instead of positive.

If the signal at input (a) is a noise signal instead of a sine wave, them the statistics of the noise must be considered. If the noise is white, then the behavior of the tracking filter depends upon the relationship between the time constants of the filter and the statistics of the noise. However, if the energy of the noise signal is peaked about some frequency, then the

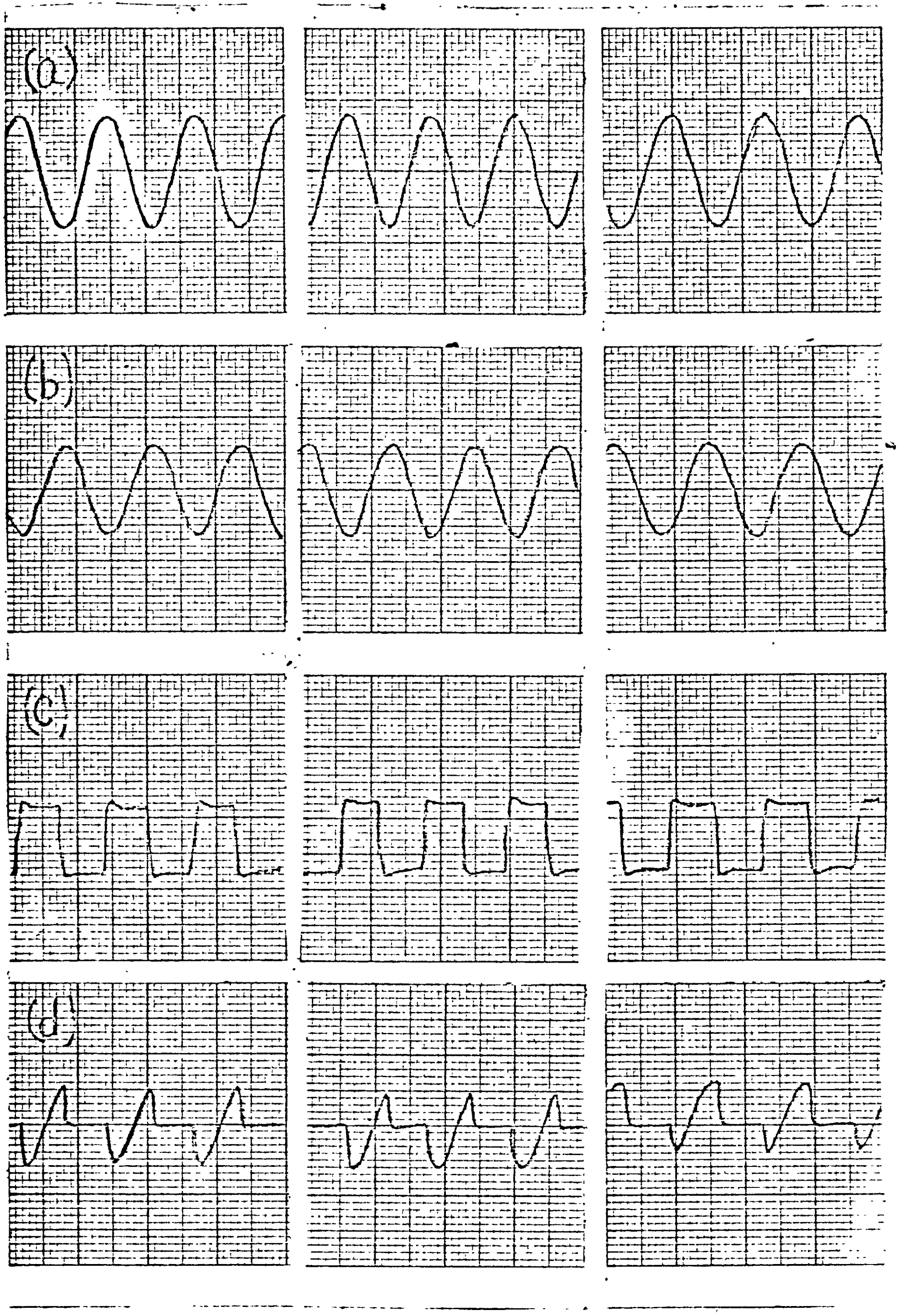

(2A)
f=f_0=8.0 cps

(2B)
f=8.4 cps

(2C)
f=7.4 cps

Fig. 4-2. Waveforms illustrating operations of frequency tracking loop. Points (a)-(d) given in Fig. 4-1. The input signal frequency is equal to (2A), above (2B), and below (2C) the tuned filter frequency.

filter will locate upon this peak, so that contributions from above and below the peak will cancel. We also expect that the tracker will display "jitter" about the peak frequency and that this jitter will decrease if we increase the time constant of the feedback loop or as the Q of the signal is increased. The feedback loop time constant is about 110 seconds.

Fig. 4-3 shows the behavior of the tracker on the natural ELF signals. Prior to taking the record the tracker had been set to a low frequency and is still being slowly tuned upwards: hence, the predominance of negative energy at point (d). The effect of the tuned circuit can be seen by comparing (b) with (a).

4.2 Q Monitor

The phase-shift principle is also used to measure the Q of an incoming signal. Whereas the frequency control uses the out-of-phase component of the input to gate the signal out of the tracking filter, the Q monitor uses the in-phase component of the input to gate the signal from the tracking filter. A high-Q signal passing through the tracking filter will undergo relatively less total phase shift than a low-Q signal. When gated by the in-phase component and time-averaged (T = 15 secs), the high-Q signal produces a net positive result which is greater than that produced by the low-Q signal.

Refer to Fig. 4-4 to see where the Q and amplitude

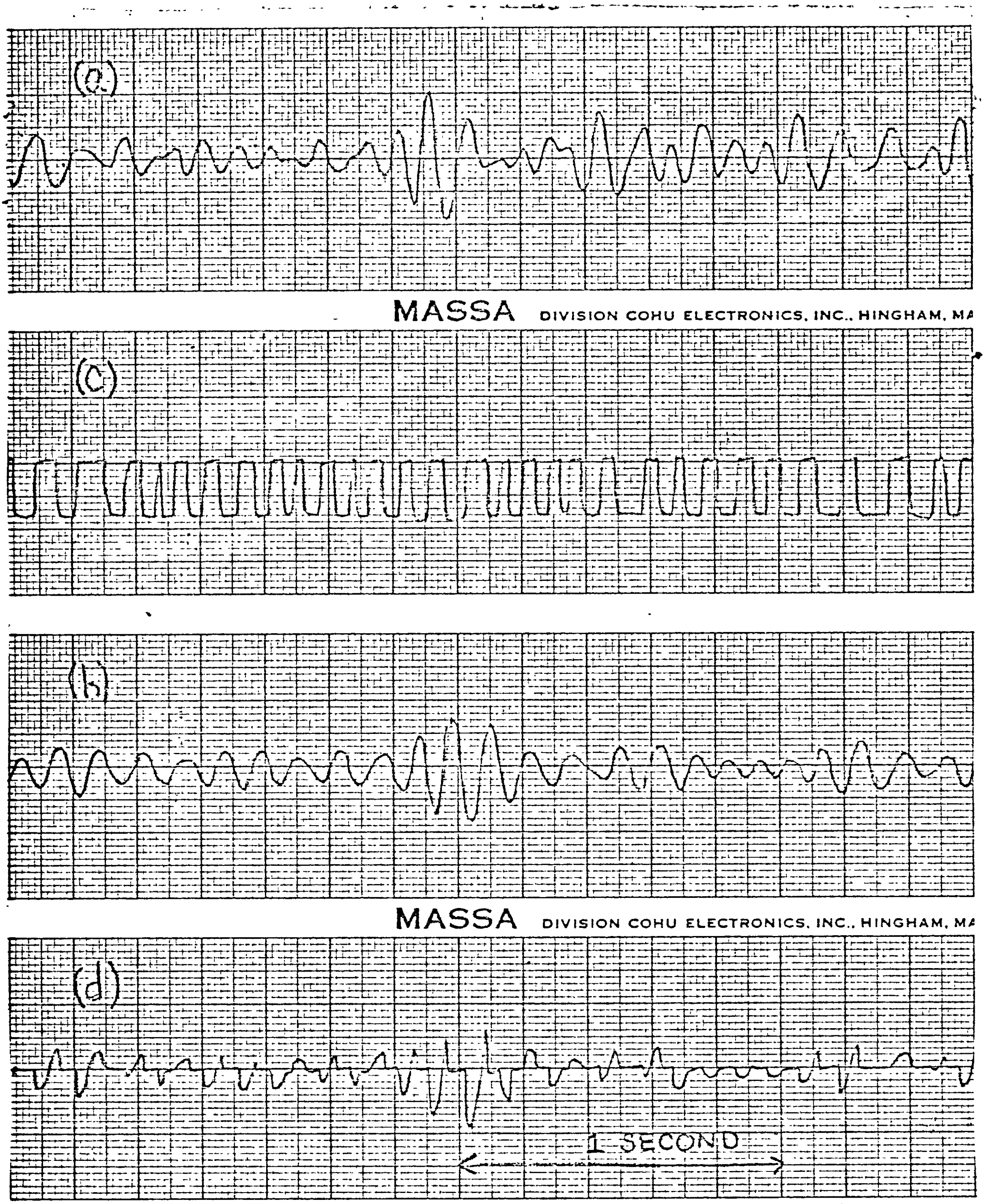

Fig. 4-3. Natural E.L.F. signal at points (a)-(d) of resonance mode tracker.

monitors fit into the resonance tracker logic.

4.3 Amplitude Monitor

The incoming amplitudes are monitored following filtering at 8.1 cps, full-wave rectification and averaging (T = 60 secs). The filter has a half-power width of 1 cps, but since the natural signals shift less than 0.5 cps and are lower Q, the filter output gives the peak frequency amplitude to within 15% at worst.

4.4 Calibration

The frequency scale is calibrated with signals from a precision oscillator. Frequency drift is less than 1% over a period of weeks.

Digital recording and analysis provide further assurance of the tracker's proper behavior and also provide calibration for the Q scale. Examples are included in the next chapter.

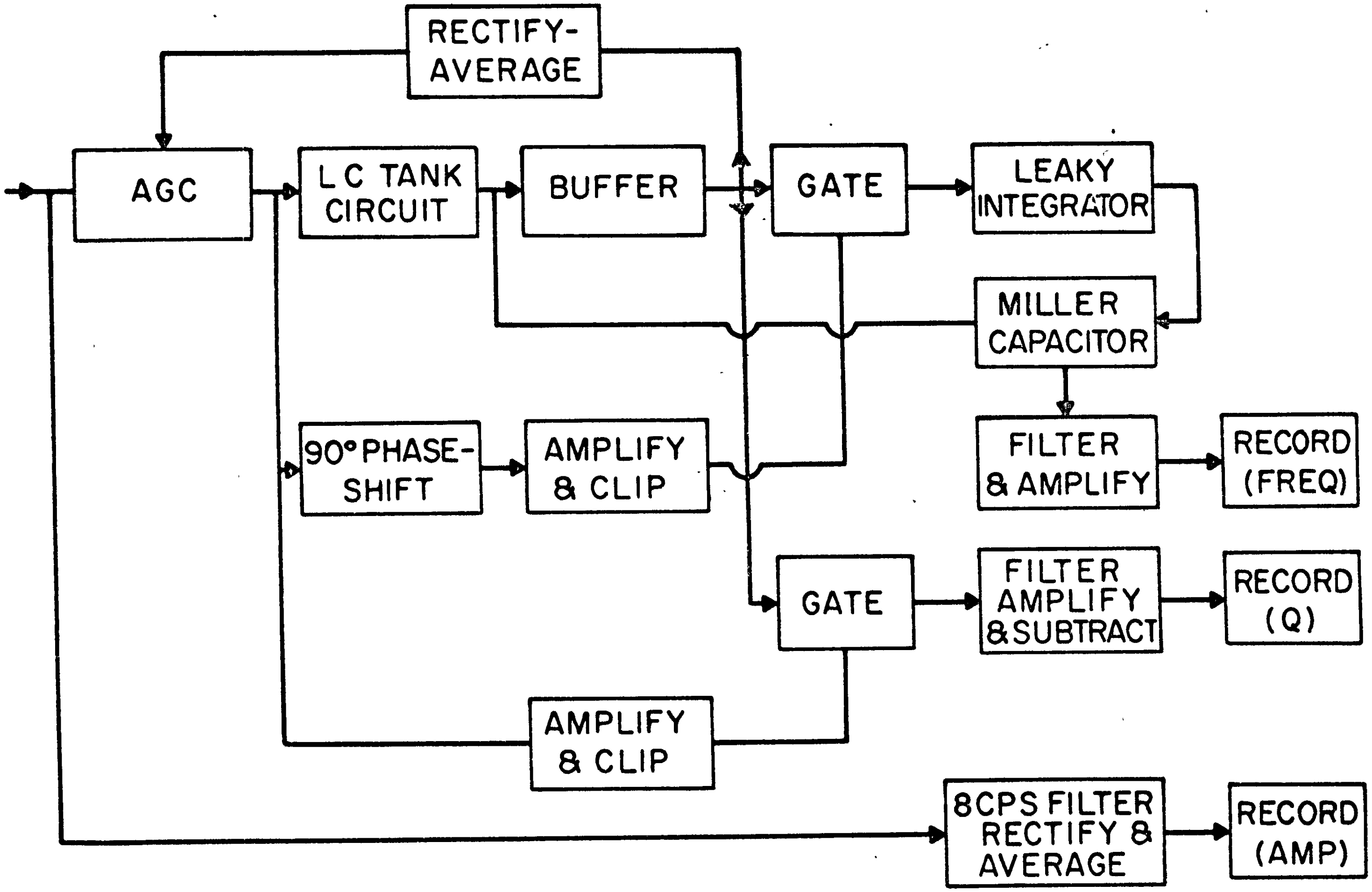

Fig. 4-4. Block diagram of the resonance mode tracker.

CHAPTER 5. FIRST RESONANCE MODE OBSERVATONS AT GROTON, MASSACHUSETTS

During 1966 and 1967 the resonance mode tracker described in Chapter 4 monitored ELF signals from a field site in Groton, Massachusetts. The equipment was in operation from June, 1966 to March, 1967 with a three monthgap from August through October due to various equipment failures and due to developmental changes in the tracker equipment. We now describe the experimental operation and look at short term and seasonal effects in the data from the tracker, In addition, we combine the tracker data with data collected previously at the Groton site to get a look (but a very incomplete look) at some long-term meteorological and ionospheric influences.

5.1 Field Site and Monitor System

The equipment and antenna used to receive ELF signals are located at the Millstone Hill Field Station in Groton, Massachusetts, operated by the M.I.T. Lincoln Laboratory. Figure 5-1 is a block diagram of the entire system. Almost all the equipment in the radome and warehouse was developed and used by Balser and Wagner in their experiments some five years ago.

Housed in a radome to shield against weather, the vertical "whip" antenna stands 5 meters high, is top-loaded, and has a capacitance to ground of 10^{-10} farads. The first amplifier is a commercially available cathode follower. The gains and band-widths of the other equipment at Millstone are given in Figure 5-1. As shown, a gain monitor records the 5 cps and 8 cps (filter bandwidth of 1/2 cps) amplitude levels at the field site. Not shown is the bank of filters and integrators used by Balser and Wagner and operated intermittently from 1962 through 1966.

After monitoring, the signals are further amplified and sent to the M.I.T. laboratory over a telephone line connection. The transmission characteristics of the line are sufficiently flat for the 4.5-10.5 cps signals, and the 8 cps amplitude level monitors at each end of the line provide a check on continuity and contamination.

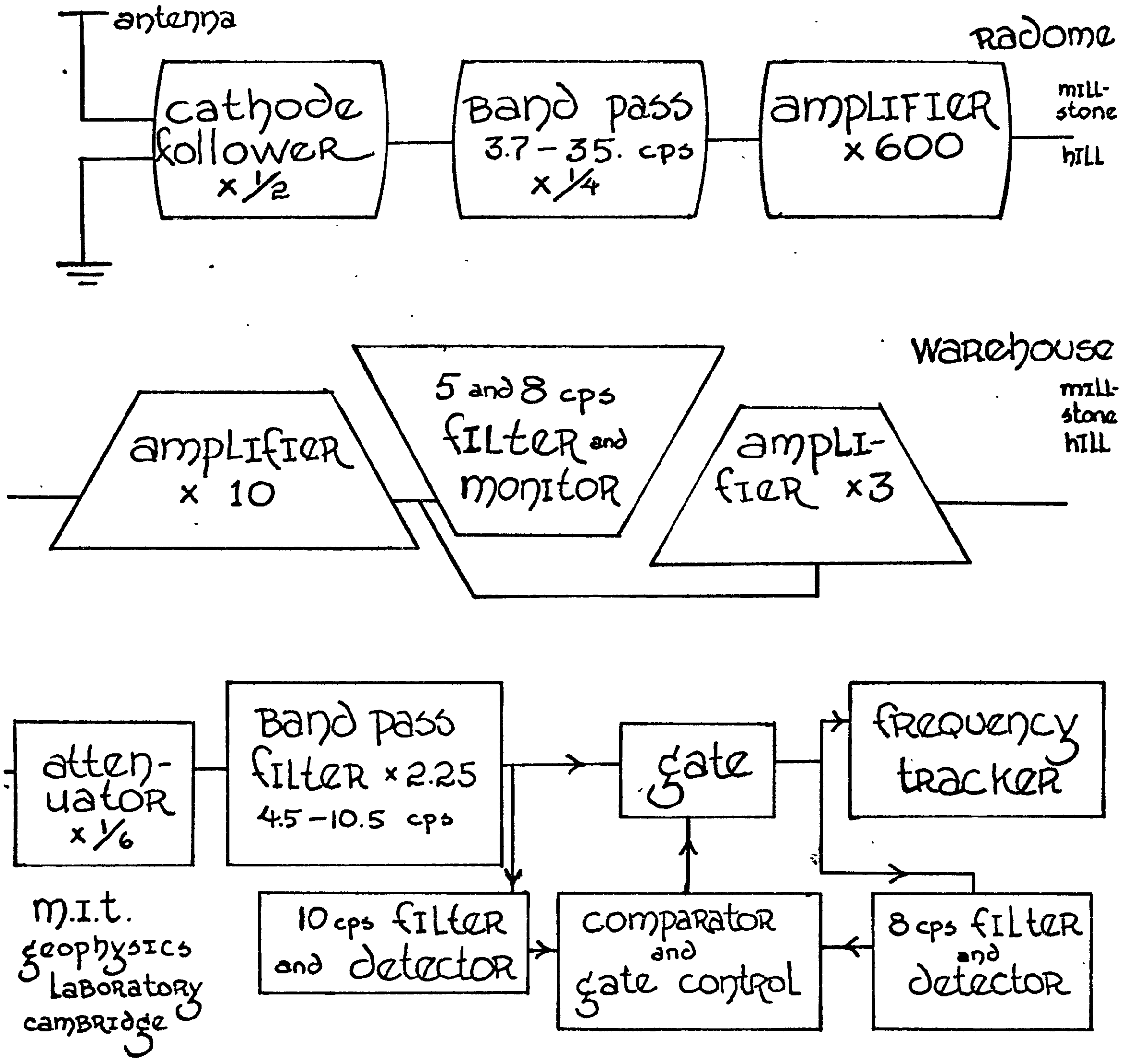

Fig. 5-1. Vertical antenna, field site equipment and laboratory equipment for Schumann frequency monitor. A direct telephone line connects the warehouse equipment to the MIT lab.

Availabilty of the signals in the laboratory proved to be a great convenience.

At the telephone line termination the signals are attentuated by 1/6, then fed into a four-pole low-pass, three-pole high-pass filter, which further limits the bandwidth fed to the frequency tracker. Circuitry and characteristics of the filter are given in Appendix B.

The ELF system quite frequently receives a 10 cps contaminating signal of obvious man-made character. As they appear at the output of the band-pass filter, these signals occur as pulses of 10 cps energy five times above background, possess a work-hour dependence, and occur less often on weekends. The bursts originate in the antenna and can not be traced to any source on the field site. Since these bursts at times occur often enough to bias the frequency tracker, they are gated out by opening the line whenever the 10cps energy rises relative to the 8 cps background. The gate control is also indicated in Fig. 5-1.

To examine correlations between cavity characteristics and magnetic activity, the telluric levels in the D.C. - 1002 cps range are also recorded. The telluric signals are picked up in New Hampshire between two electordes some 75 kilometers apart and sent to the laboratory at M.I.T. over telephone lines. This provides a reliable scaled indicator of geomagnetic activity.

System noise is checked periodically by shorting the cathod-follower input with a capacitor equivalent to the antenna-to-ground capacitance.

5.2 Resonance Mode Tracker Data

Figure 5-2 and 5-3 exhibit 16 days of peak frequency, amplitude and Q data, along with low frequency (D.C.-.002 cps) tellurics. Time is eastern standard. Before photographic reduction, the chart scale was 1/4 inch per hour.

The amplitudes typically begin to rise at 0600, peak first between 1000-1200 (African thunderstorms) and again between 1400-1500 (South American thunderstorms) and decrease to nighttime levels at 1800. Note the day-to-day shifts of relative amplitudes of the morning and afternoon peaks.

The peak frequency drops at 1200 from morning levels of 8.4-8.6 cps to afternoon levels of 7.9, then begins to rise in the late afternoon. The frequency trend from 0600 to 1800 is much more consistent on a day-to-day basis then it is during the nighttime hours. This is because the storm patterns as observed in Massachusetts during winter are strong and consistent during the day, as is evident in the amplitude data. During the night the thunderstorms are low intensity and scattered geographically. Their geographical variability from night to night explains the lack of consistency of the

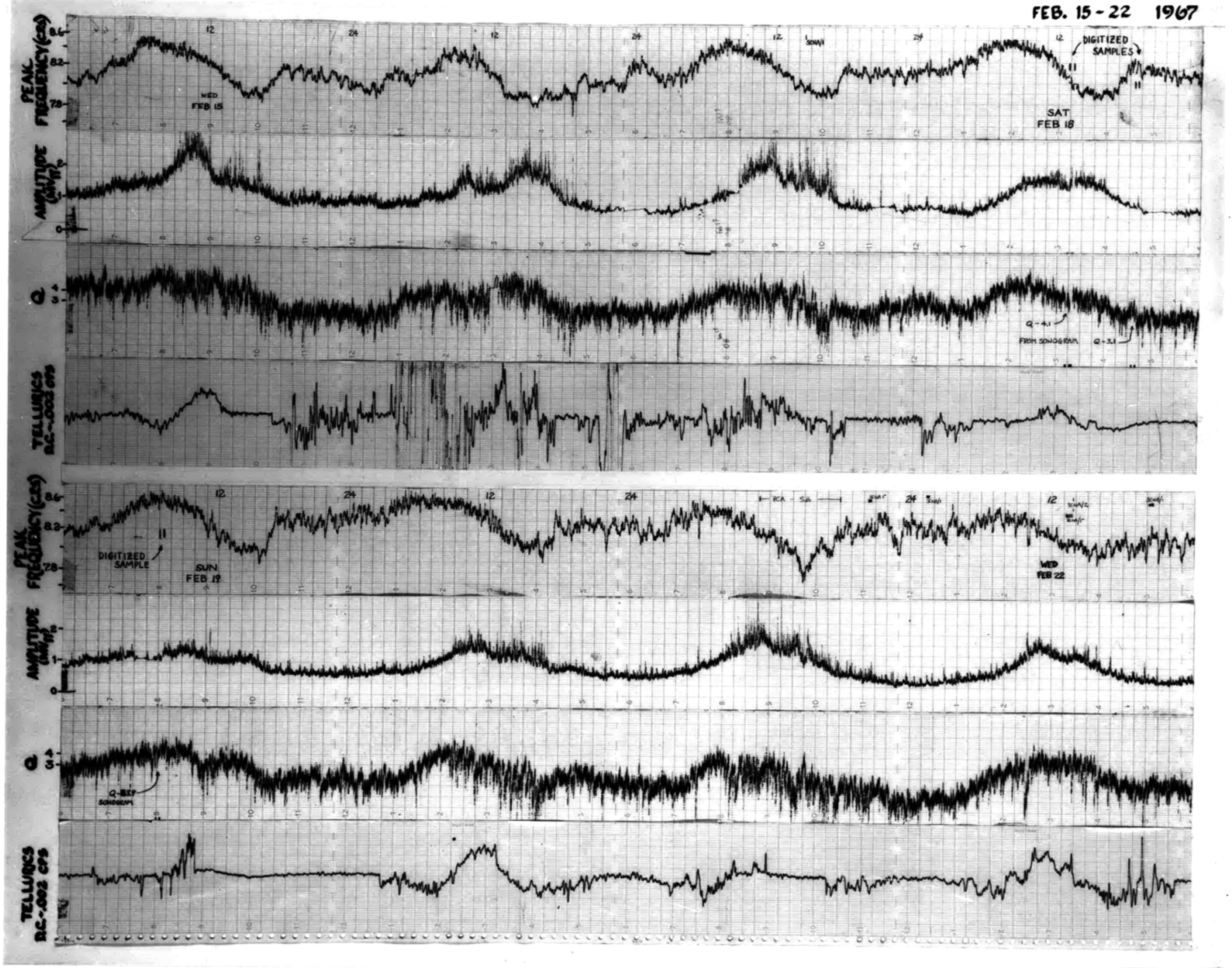

Fig. 5-2. Eight days of peak frequency, amplitude, and Q from resonance tracker. Low frequency tellurics indicate magnetic activity level. On the amplitude scale, $1 mv_{pp}$ corresponds to 0.1 mv/meter/cps.

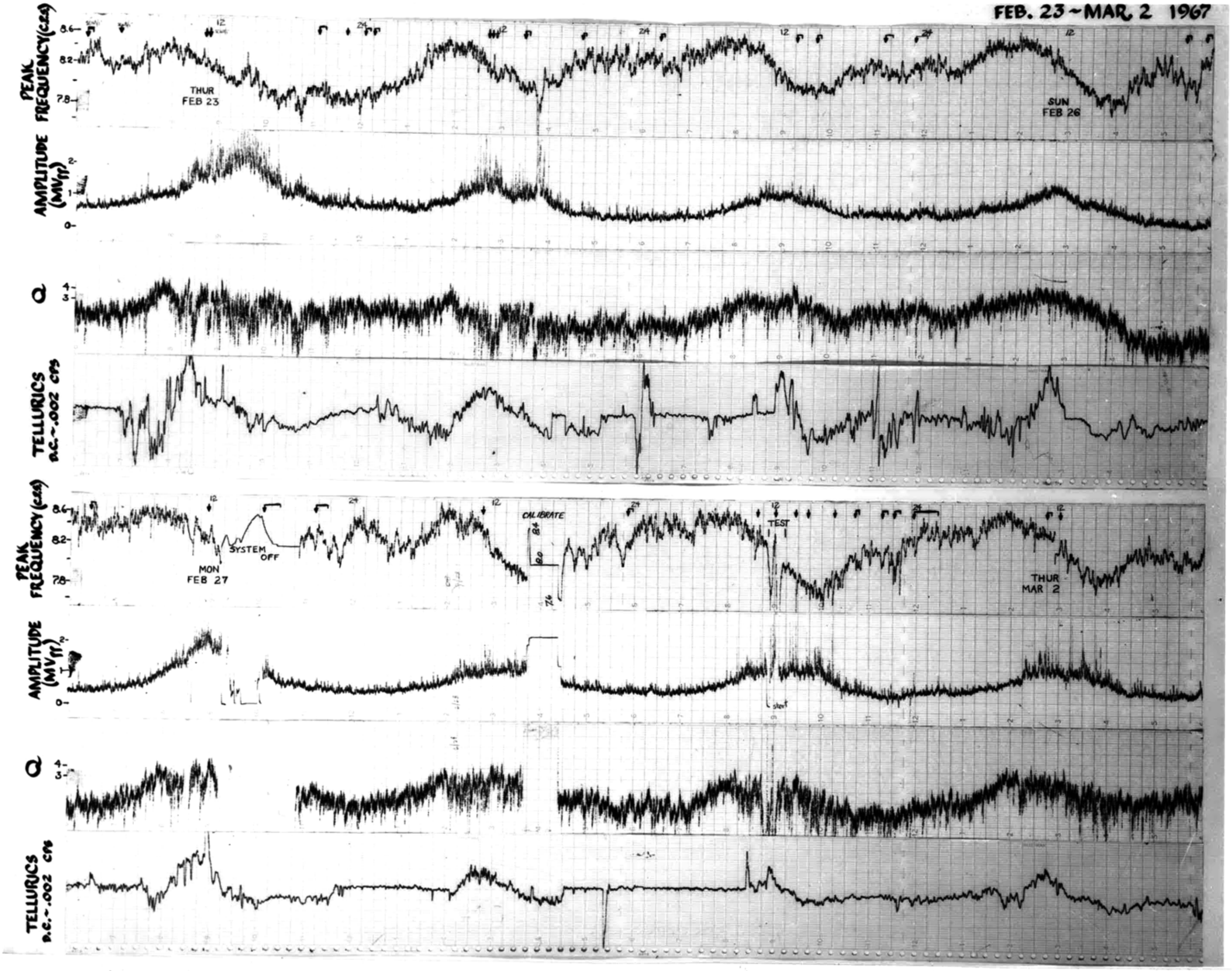

Fig. 5-3. Continuation of Fig. 5-2. Arrows denote SID activity.

frequency variations. Their low intensity results in a lower observed Q since the cavity energy is decreased relative to whatever non-cavity energy may be present. The lower Q causes the increased jitter on the frequency record during the nighttime.

Digital analysis of the Schumann band provides a check on the frequency tracker. The three digital dynamic spectra or sonograms in Figure 5-4 were taken at the times indicated on February 18 and 19 in Figure 5-2. For these examples the output of the automatic gain control of the tracker fed the digitizer, so both digitizer and tracking circuitry look at the same signal. Each line in Figure 5-4 represents a 3.3 minute protion of the three 10-minute samples. The "T" gives the frequency reading of the tracker during the ten minute sample. In the second sample an arrow indicates the increasing frequency reading of the tracker during the ten minutes, in agreement with the upward shift of the three sequential sonogram spectra.

We see good agreement between the tracker and the sonogram estimates of the peak in all three cases. By averaging the Q's of the sonogram spectra we obtain a calibration of the tracker's Q monitor, as indicated in Figure 5-2. Although the peak frequency changes by 0.5 cps between the first and third samples, both tracker and digital sonograms give identical Q's assuring us that the Q estimate is frequency-independent.

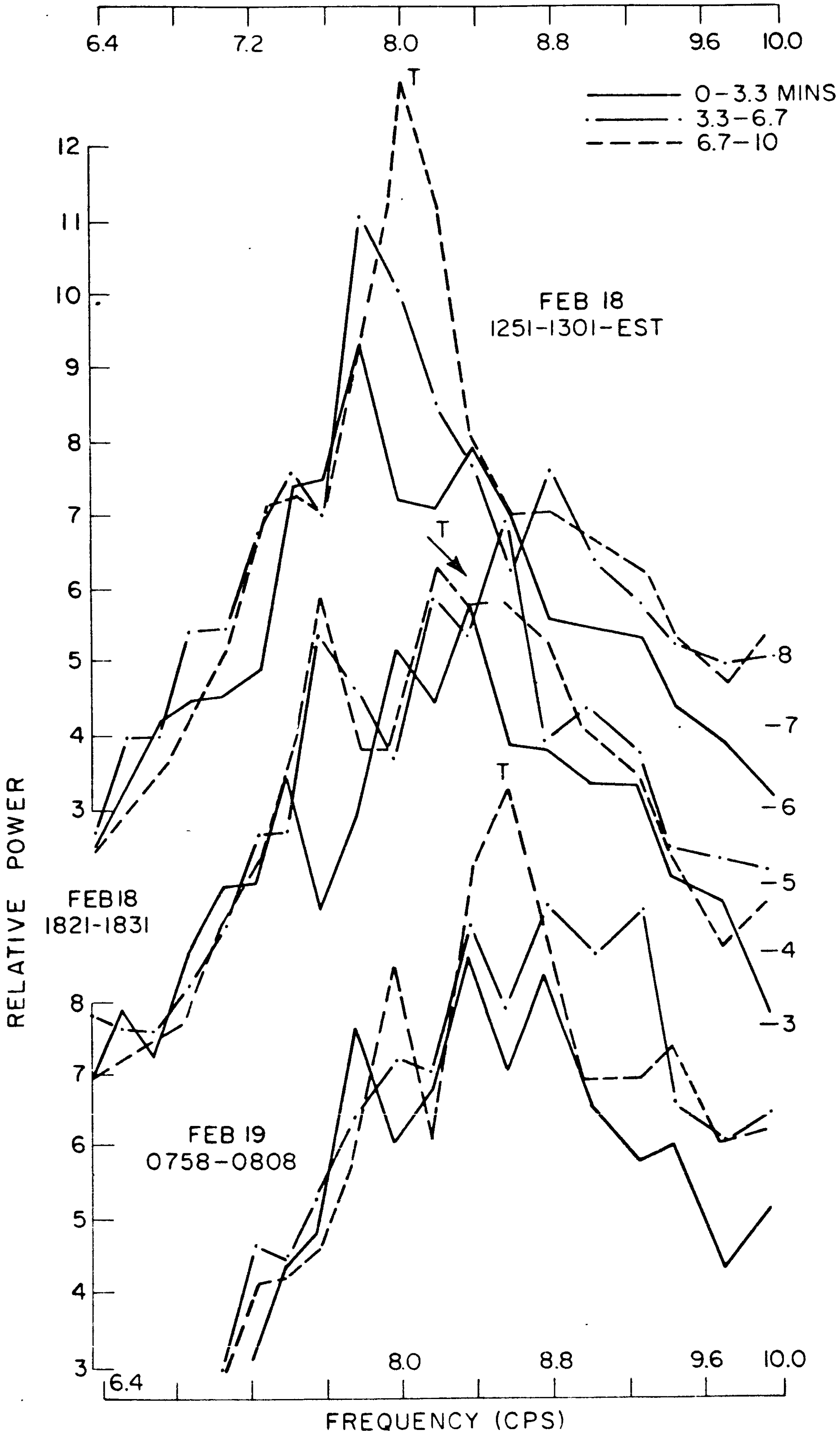

Fig. 5-4. Digital sonograms at times indicated in Fig. 5-2.

5.3 Transient Effects Associated with Geomagnetic and Ionospheric Disturbances

Variations Associated With Magnetic Storms

We have plotted in Fig. 5-5 three months of smoothed Q and frequency data from the tracker, along with the Fredericksburg K index. The data of Figs. 5-2 and 5-3 are condensed into the bottom two lines of Fig. 5-5.

The most striking feature of Fig. 5-5 is the strong diurnal variations of both frequency and Q. Because the shape of the diurnal is caused by a mixture of source and ionospheric effects, we have not attempted to remove the diurnal trend.

Let us first examine the effects of some isolated magnetic storms. The sudden, brief storm of Feb. 15-16 is a good starting place since the event can also be examined in Fig. 5-2. As is clear from the data the peak frequency is reduced during the magnetic storm. The Q, however, attains higher values some 24 hours before the storm onset and remains high for several days afterwards. Another feature is the reduction in the diurnal frequency swing between its maximum at 0800 and its minimum at 1400. This occurs in other cases where the Q is enhanced during a magnetic storm, but does not always occur simply because the Q is high. The magnetically quiet period of Jan. 28-Feb. 2, is such an exception to the high Q, low diurnal variation association.

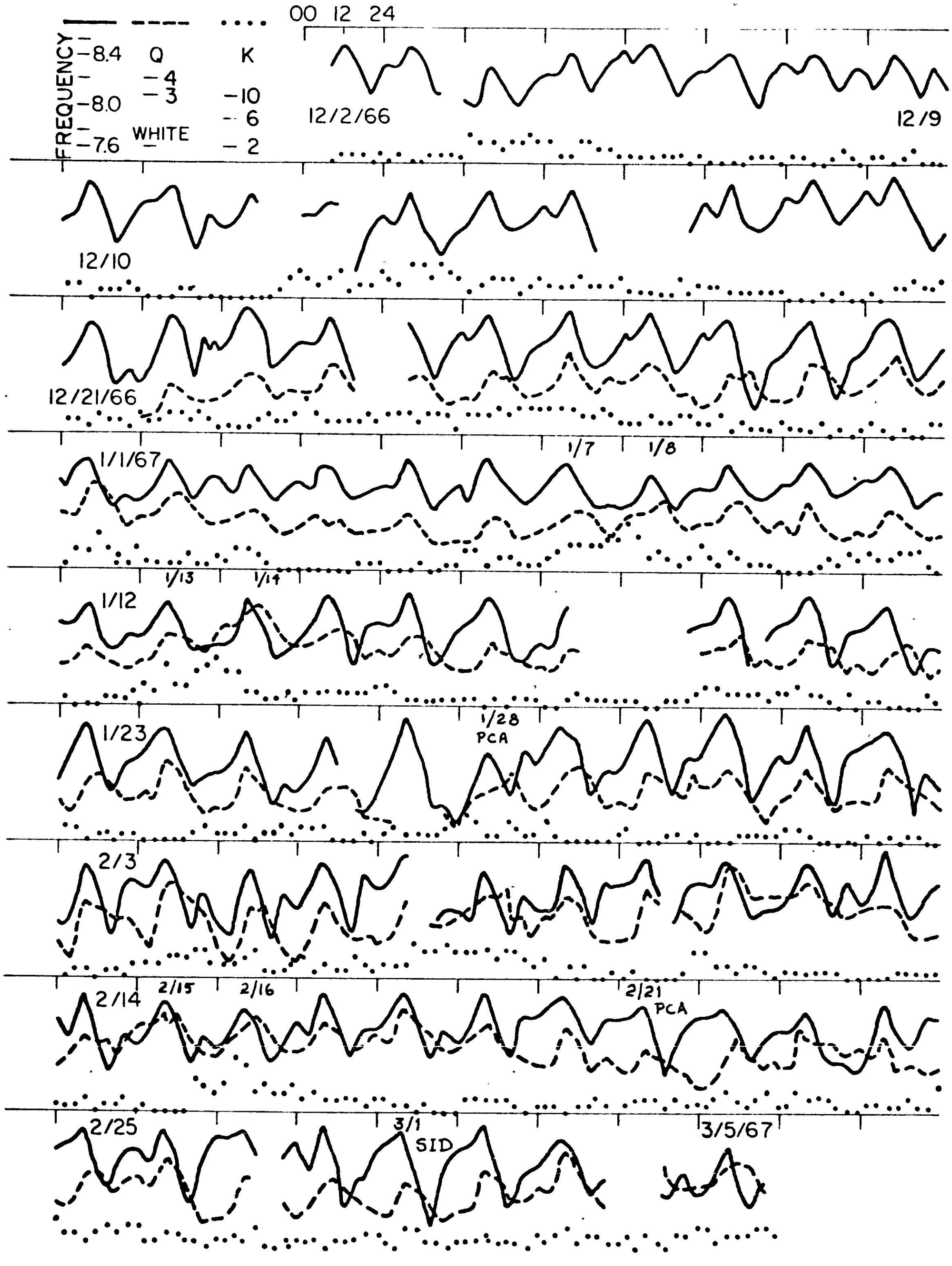

Fig. 5-5. 94 days (Dec. 2, 1966-March 5, 1967) of peak frequency (solid line), Q (dashed line) and K_p (dots). Time is eastern standard. Scales at upper left. The Q scale applies after January 27.

The magnetic storms of Jan. 7-8 and Jan. 13-14 are discussed next since these two events are both isolated and intense. In both cases the Q rise begins roughly at the storm onset and attains its maximum within the 24 hours after the storm maximum; this time sequence of Q behavior differs from that of the Feb. 15-16 storm. The reduction of peak frequency during Jan. 8 is similar to that of Feb. 16, although the Jan. 13-14 storm produces no reduction of peak frequency. During both January storms the peak frequency swing is reduced concurrent with the rise of Q.

When high magnetic activity lasts for a number of days, as it does during Dec. 21-29 and Feb. 4-8, the cavity behavior can not be characterised as it can during isolated storms.

For convenience we have tabulated in Table 5-1 the cavity response during the times of high magnetic activity by examining periods in Fig. 5-5 when the K index exceeded 3. Note that the magnetic storms are best correlated with Q increases. If we refer to Table 5-2 we see a plausible explanation of why this is so. If increased ionization in the E-region characteristically accompanies increased storm activity, then the table indicates an overall Q increase, since both day and night ionospheric profiles give Q increases. For the frequency change the overall effect is mixed, since day and night profiles produce opposite frequency changes,

	Dec. 1966			Jan. 1967				Feb. 1967		
K≥4	4	13-14	24-26	1	7-8	13-14	28	4-8	10-11	15-16
Δ Diurnal Frequency Max.	-	-	0	0	-	0	-	0	0	-
Δ Diurnal Frequency Min.	-	-	+	0	0	0	-	0	0	0
ΔQ	-no data-		+	+	+	+	0	+	+	+

Table 5-1. Days when Fredericksburg K≥4 with response of cavity peak frequency maximum (∿0800 EST) and minimum (∿1600 EST) and Q taken from Fig. 5-5. A plus indicates an increase, a minus a decrease. A Δfrequency entry indicates a change of 0.1 cps or more , a ΔQ entry indicates a change of 1.0 or more.

Perturbation of Electron & Ion Densities									First Mode Changes		
30	50	70	90	100	150	200	270	300	Δf	ΔQ	
x2	x2	x2							-.18	-1.3	DAY
		x1.5	x3	x4	x3				+.10	+1.3	
x2	x2	x2							-.43	-0.3	NIGHT
			x3	x4	x3				-.36	+2.9	
						x3	x25	x8	-.46	-0.6	

Table 5-2. Effect of ionospheric density changes upon first mode resonance models (from Table 7 of Madden and Thompson).

although the nighttime reduction is greater for equivalent ionization increases. We see that changes in the lower ionosphere are ruled out, since both day and night perturbations give Q decreases, contrary to what we observe. This interpretation is consistent with the known ionization effects of magnetic storms.

Hourly ionosonde data were available for the period Feb. 17-Mar. 2, but comparison with the tracker data failed to uncover any consistent relationships between cavity parameters and f_oF_2 (F_2 layer critical frequency of the ordinary wave) or f_{min} (lowest observable frequency). Although a more extensive evaluation would be wise, this lack of consistency is indicative of the problems which arise when we try to compare cavity results, which are influenced by world-wide ionospheric conditions, with measurements influenced by local ionospheric conditions.

A helpful aid in understanding the tracker information will be a more detailed catalog of first mode changes than that available in Table 5-2.

Variations Associated with PCA and SID Events

We now examine some cavity effects associated with D-region ionospheric events. The term "polar cap absorption" (PCA) refers to the blackout of radio communications over the polar cap which occurs when energetic protons cause increased ionization over the polar areas.

More extensive descriptions of PCA and SID will be found in the references cited in Chapter 1.

PCA events occur rather rarely and only three PCA have occured thus far during tracker operation. The results of a PCA on Feb. 21, 1967 can be examined in Fig. 5-2. On that day the cavity peak frequency decreases markedly and the Q decreases moderately concurrent with a PCA event of -5db. Another PCA event occurred at 1000 EST on January 28, 1967 (see Fig. 5-5). The peak frequency began to drop below the values of the previous day some 10 hours before PCA commencement. By the time of commencement, the frequency was 0.4 cps below the previous day's value. The Q during this period is somewhat less than the Q at the same hours on the following days. Unfortunately the Q monitor was altered on Jan. 27 so comparisons with the previous days are not possible. The third instance of PCA-associated effects occurred at 2030 EST on July 6, 1966 (not shown). During a one hour period spanning the PCA event, the peak frequency dropped 0.2 cps and the Q also dropped. Frequency and Q returned to normal values after the one hour excursion. The primary result here is that the Q decreased and the peak frequency dropped dramatically in all three PCA events.

Scattered throughout the 16 days of data in Figures 5-2 and 5-3 are numerous SID events reported by the High

Altitude Observatory. These sudden ionospheric disturbances are caused by ionization changes on the earth's daylight side, and are subclassed as sudden enhancement of atmospherics (SEA), sudden cosmic noise absorption (SCNA), or sudden phase anomaly (SPA), according to the manifestation observed. In Figure 5-2 the subclasses are labeled; in 5-3 all events are denoted by a downward arrow.

Contrary to expectations, the cavity peak frequency does not respond to the individual short-lived SID events, or at best any systematic cavity changes are buried in the normal fluctuations. However, during February 23 and the first five hours of the 24th, the peak frequency drops well below its usual diurnal values while several ionospheric events occur. This particular case is confused by the magnetic activity and the higher-than-normal Q values. The data of March 1 give a clearer picture: the peak frequency drops significantly and the Q drops slightly while the magnetic activity is quiet and several ionospheric events occur. Thus it appears that SID may have a cumulative effect on the cavity resonance while individual events alone fail to produce discernible frequency or Q effects.

Both SID and PCA are D region events; they differ in their location and in the nature of the ionizing energy. Table 5-2 shows that both the first mode frequency and Q decrease when D--region ionization is doubled. This is what we have observed during three PCA and during one period of several SID. From the SID-associated data it appears that the SID model used for Fig. 3-3 was too strong: the model predicts a frequency reduction of 0.6 cps, while we observe a 0.2-0.3 cps reduction. Fig. 6-2a shows a frequency reduction of 0.2 cps for a 20% phase velocity decrease over the polar caps (a complete PCA model would also contain a Q reduction). This result is in quantitative agreement with the Feb. 21, 1966 PCA event.

With data from only one station we have not attempted to evaluate the extent of the D--region events. In Chapter 6 we explore such possibilities for the case when several simultaneous cavity measurements are available.

Seasonal Variations

The frequency tracker operated continuously through June, July and August, 1966, and again from early

November, 1966 until early March, 1967. From this data (Figs. 5-6 and 5-7) we can look at summer-winter frequency and amplitude trends. In the following paragraphs we will refer to the predicted frequency and amplitude diurnal trends for June and December, as given in Fig. 3-7.

Our first remarks concern some of the general pictures of Fig. 5-6. The frequency patterns are remarkably consistent on a day-to-day basis indicating that thunderstorm positions are fairly stable over several days time. The monthly changes in the frequency patterns are of course due to the seasonal shift of the thunderstorm locations. Referring to Fig. 3-7, we see that some of the 1966 frequency data is higher than the frequencies predicted by the D11-N12 model. The changed average frequency does not affect the use of model results in interpreting perturbation changes or diurnal variations, however.

Referring next to the amplitude patterns in Fig. 5-7, we note that the June examples are characterized by a broad maximum around 1600, caused primarily by North American storms. In July and August the afternoon maximum occurs a few hours later and the morning maximum occurs a few hours earlier. The summer data differs from the predicted patterns only by requiring a greater African contribution than expected. The November and December amplitudes lack the characteristic double maxima of the February (Fig. 5-2) data. Again the predicted African contribution is lower than observed. East Asian

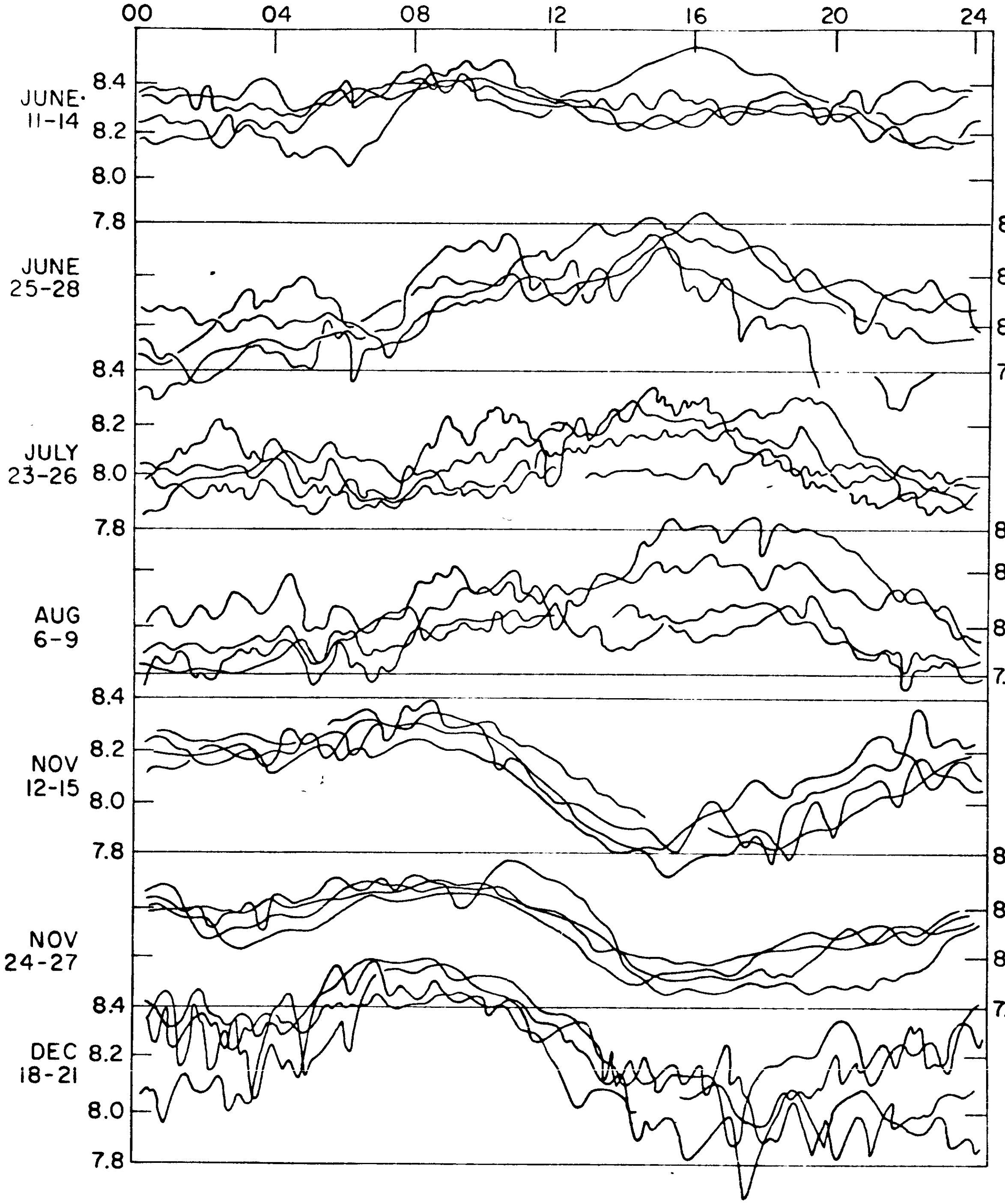

Fig. 5-6. Tracings of diurnal frequency variations from the resonance tracker during 1966. Time is eastern standard.

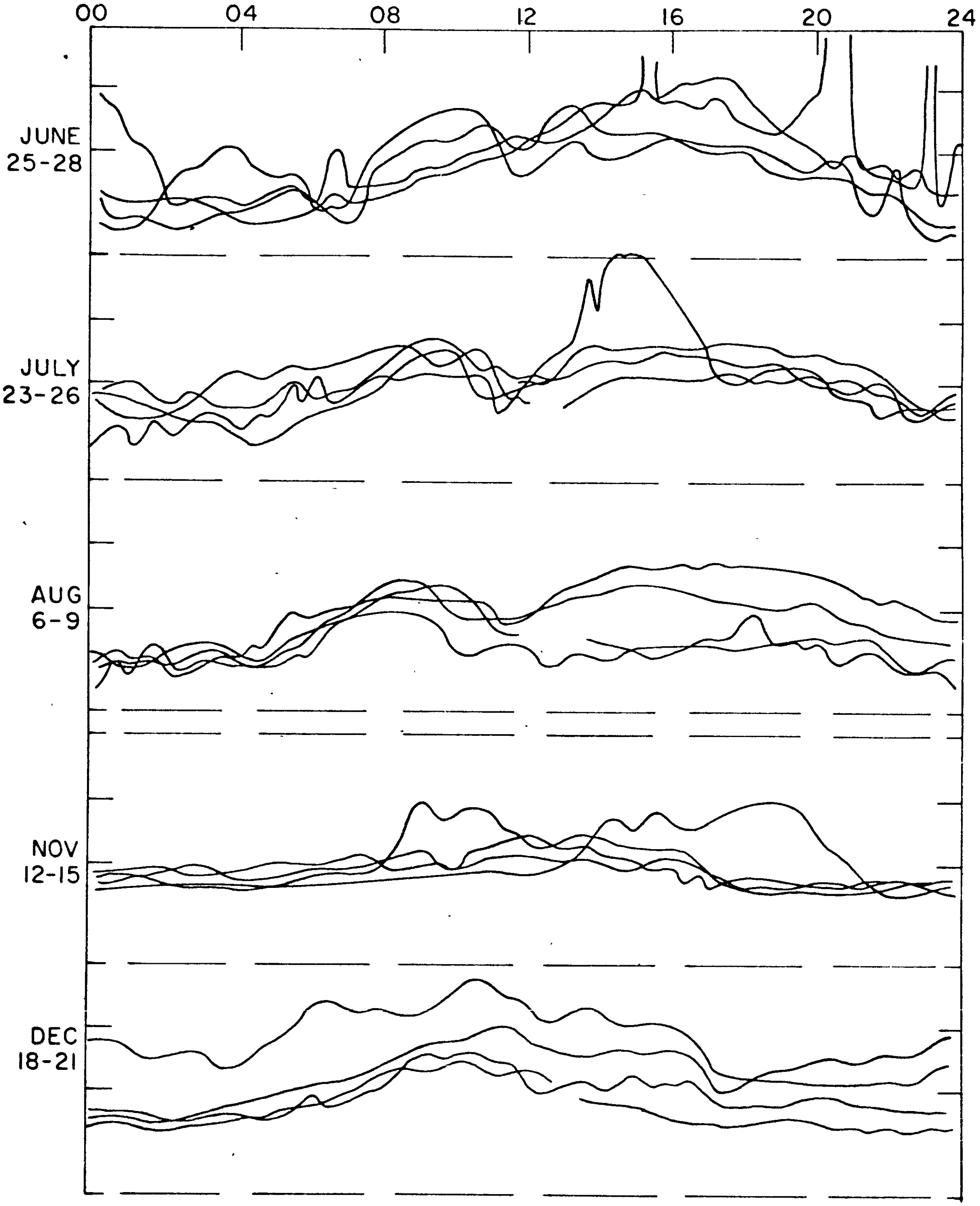

Fig. 5-7. Diurnal amplitude tracings at 8 cps during 1966, supplementary to Fig. 5-6. Center of scale is roughly $1 mv_{pp}$. Equipment altered in October.

(0400 EST) storms do not give a consistant contribution in any season.

We now consider Fig. 5-6 again to compare the frequency variations with the predictions. In the summer months the frequencies decrease after 1600 in accordance with predictions based upon thunderstorms in the western U.S. In the winter the frequency maximum at 0800-1000 in the place of the predicted minimum suggests that West African storms have supplanted the expected East African storms. The observed frequency decrease during the winter afternoon appears quite plausible from the predictions of Fig. 3-6 as South American sources replace the West African sources. Clearly we require a firmer knowledge of storm locations to make this explanation completely satisfactory.

5.5 Observations Over a Six Year Span

Enough data has been collected at the Millstone Hill station over the past six years to examine some long-term effects (Fig. 5-8 and 5-9). Although three techniques of analysis have been employed, the preamplifier, filters, and amplifiers at Millstone were installed in 1962 by Balser and Wagner and have not been changed.

The 1961 data, from Balser and Wagner's original research (1962a, 1962b), were obtained with magnetic recording and digital analysis techniques. The 1962-1964 data were reduced from the output of an analog

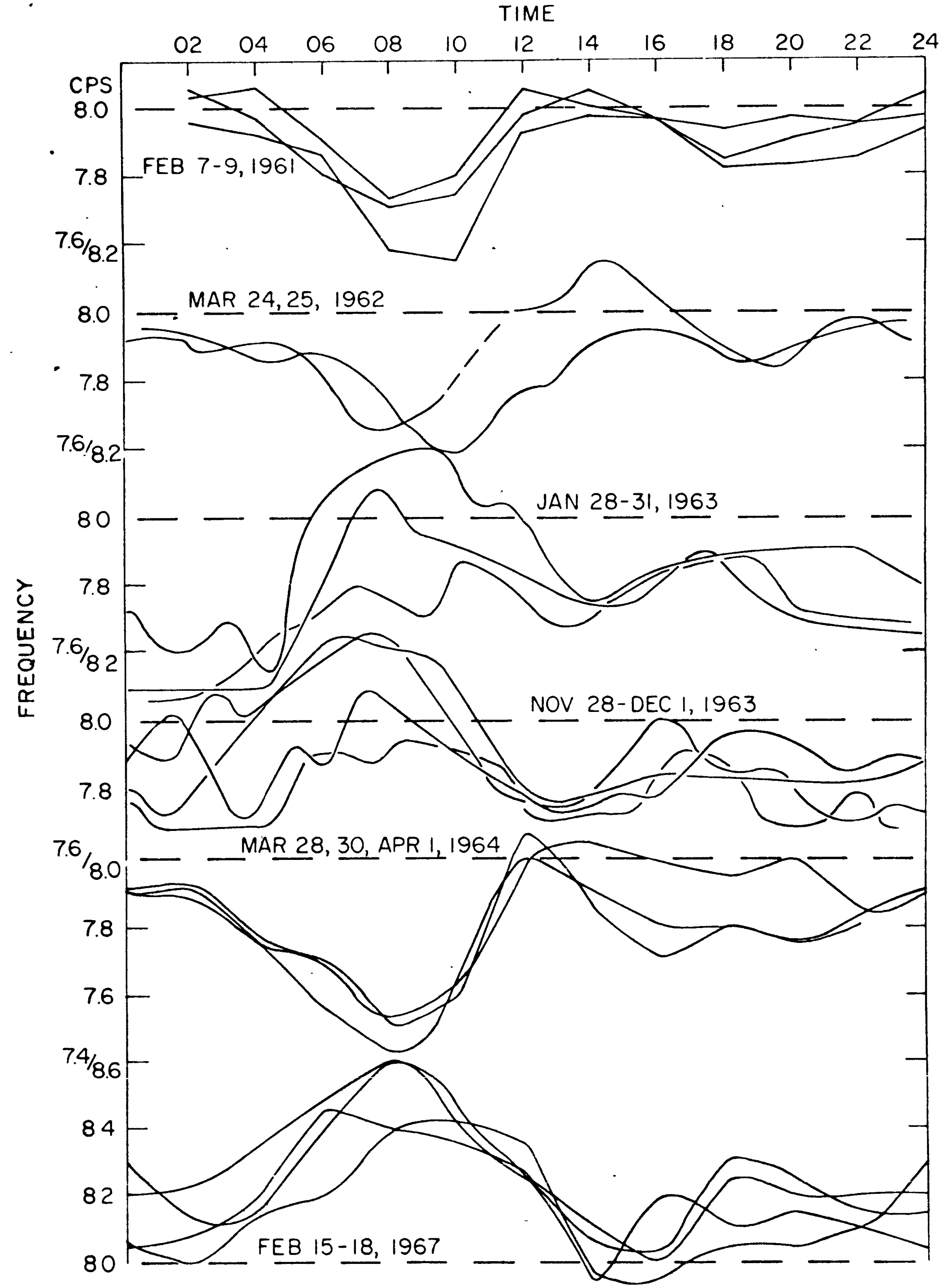

Fig. 5-8. Diurnal frequency variations of first cavity mode spanning years 1961-1967. 1961 examples-Balser and Wagner digital analysis of 12 minute sample taken every two hours. 1962-1964 examples-consecutive 15 minute integrations on Balser-Wagner analog filter bank. 1967 examples-resonance mode tracker.

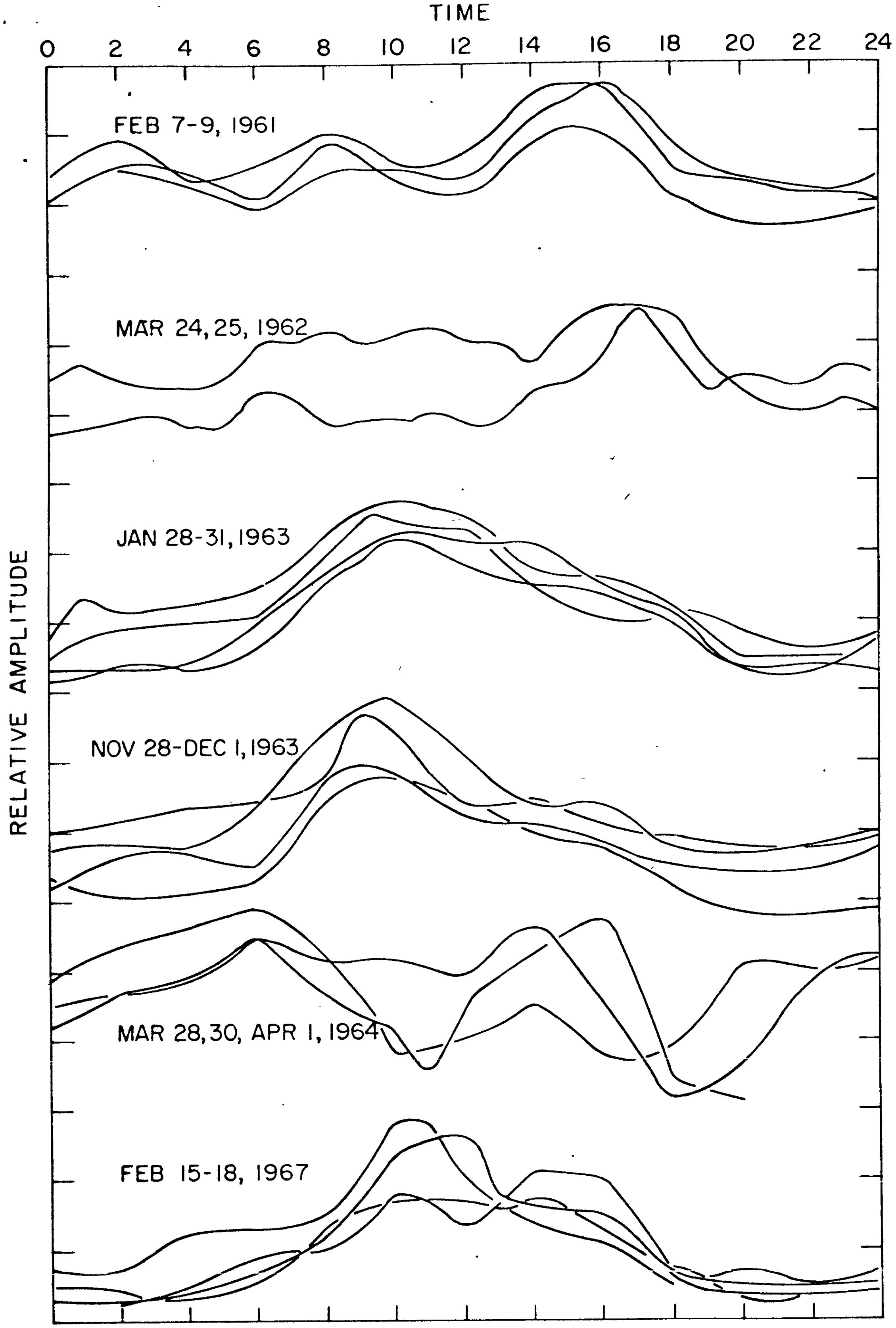

Fig. 5-9. Diurnal amplitude variations of first cavity mode, supplementary to Fig. 5-8. Vertical scales arbitrary, do not make quantitative comparisons among the five scales. Time is eastern standard.

filter bank described by Balser and Wagner (1964). Data from this system is fairly complete during March, April, and May, 1964; the 1964 examples presented here are representative. The February 1967 data were taken from Fig. 5-2.

The most striking feature of Fig. 5-8, the 0800 peak frequency dip on the 1961, 1962 and 1964 data versus the 0800 maximum on the other data, must be explained entirely on the basis of source positions. Looking at Fig. 5-9 we see that the 1961, 1962, and 1964 amplitude data have a diurnal pattern quite different from the other three examples. The 1961, 1962, and 1964 amplitude peaks and the frequency dips at 0600-0900 are undoubtedly due to storms off Southeast Africa. In the other three examples the reversed features are best explained by a large number of storms in West Africa, along with a lack of Southeast Africa storms. The large area and great intensity of West Africa storms would offset the effect of their null positions relative to Massachusetts, and the West Africa position would place it on the high frequency edge of the model results (Fig. 3-6).

A significant trend in the long-term data is the average frequency increase in 1966-1967. It is quite doubtful that this net increase could be due to source effects. On the other hand it is difficult to tie in the trend with solar control. Cosmic ray activity in 1967 was not significantly different from 1963. Although sunspot activity did decrease during 1963-1964, the sunspot numbers indicate comparable activity during the 1961 and 1967 samples. Hopefully consistent monitoring will yield a better picture of long-term trends.

CHAPTER 6

AN APPROACH TO THE INVERSE PROBLEM FOR SCHUMANN RESONANCE DATA

The inverse problem for the Schumann resonance may be posed as follows: given a number (a dozen or so) of stations observing first mode amplitude, peak frequency, and Q, what information might we be able to deduce concerning a) the location of sources and b) the location, vertical extent, and intensity of those ionospheric perturbations which influence the resonance. "Locating" a source will involve areas of 20° by 20° or more; "locating" an ionospheric event will involve areas on the order of an eighth of the earth's surface. As one might expect, increased geographical coverage (wide-spread stations) and increased amounts of data (more stations) will make possible more accurate solutions and/or reduce the zone size of the solutions. We limit our considerations here to the first cavity mode, since spatial information is more useful than coverage of the higher order modes. Since world-wide resonance data is of course now unavailable, the possibilities outlined in this chapter are conjectural.

6.1 Location of Thunderstorm Sources - Technique

We consider the problem of using received power at the peak frequency from a number of stations to determine the location of the cavity excitation. Since the sources are probably thunderstorms, we make use of the known storm-day maps (Handbook of Geophysics) to narrow our choice somewhat. The problem is stated as the solution of:

$$\begin{bmatrix} R_{11} & R & \ldots R_{1m} \\ R_{21} & & \\ \cdot & & \\ \cdot & & \\ \cdot & & \\ \cdot & & \\ \cdot & & \\ R_{n1} & & R_{nm} \end{bmatrix} \begin{bmatrix} S_1 \\ S_2 \\ \cdot \\ \cdot \\ \cdot \\ S_m \end{bmatrix} = \begin{bmatrix} V_1 \\ V_2 \\ \cdot \\ \cdot \\ \cdot \\ \cdot \\ \cdot \\ V_n \end{bmatrix} \qquad (6\text{-}1)$$

where

S_i	$i=1,\ldots,m$	are the source zones of storm location.
V_j	$j=i,\ldots,n$	is the power received at the n stations.
R_{ij}		represents the matrix of Green's functions linking the source at i to response at j.

The matrix R is computed simply by taking the V^o response (see eqn. 2-9) at the j stations for a source at one of the i zones, then repeating for the rest of the i zones. Using the V^o response instead of the V' response makes R independent of local time and is quite adequate since the variations in the two amplitude patterns differ by only a few percent. Another simplification results from the low Q nature of the cavity, which makes it possible to consider the amplitude response at a fixed frequency, say 8.0 cps, to representative of the amplitude at the peak frequency. Since the V_j will include experimental error, it is expedient to take n greater than m.

If there were no complicating factors we could solve eqn. 6-1 using standard techniques for solving a set of overdetermined simultaneous equations. However, a major complication arises in the computation of R. The Greens functions which form R have both amplitude and phase; in R itself the phase is discarded since the cavity excitation is a noise source. The lack of phase information manifests itself in two ways when it comes to solving 6-1. Since the pattern of the power distribution in the source hemisphere is very similar to the pattern in the antipodal or opposite hemisphere, we are unable to distinguish the two without phase information. As we will see in an example this forces us to restrict the zones of possible solution by relying upon known thunderstorm distributions. Also the lack of phase information means that negative source solutions cannot be allowed. This second handicap imposes a non-linear constraint upon the solution of eqn. 6-1.

To solve 6-1 while holding the vector S_i positive, an iterative technique was adopted. In this procedure an initial "guessed at" S_i is operated on by R and the result is compared to the observations V to obtain an error value. To each S_i value some fraction of S_i is then added or subtracted, provided that the new RS product reduces the error value. This operation continues until the error is small enough. Results obtained using this technique on a digital computer for 15 x 10 R were both satisfactory and economical.

6.2 Location of Thunderstorm Sources - Numerical Example

The upper portion of Figure 6-1 shows the geographical locations for a set of hypothetical receivers and possible source locations for a numerical inversion experiment. The 10 S_i source solution zones (numbered squares) correspond to South American, African, and Asian storm centers. The 15 V_j "receivers" (encircled numbers) are scattered around the earth. The heavily outlined $40^o \times 20^o$ area in both upper and lower portions of the figure encloses the source area.

Coefficients of the R matrix were determined as explained in the preceding section. The 15 observed V_j's were produced using the approach for V^o described in Chapter 3, with the source in the heavily outlined area. Note that the "experimental" source and the areas sought through inversion do not completely overlap. To further test the iterative technique, 10% errors were added to and subtracted from the observed V_j's.

The iterated S_i solution is shown in the lower half of Fig. 6-1; a perfect solution would show all the source in squares 8 and 9. Ten percent of the source

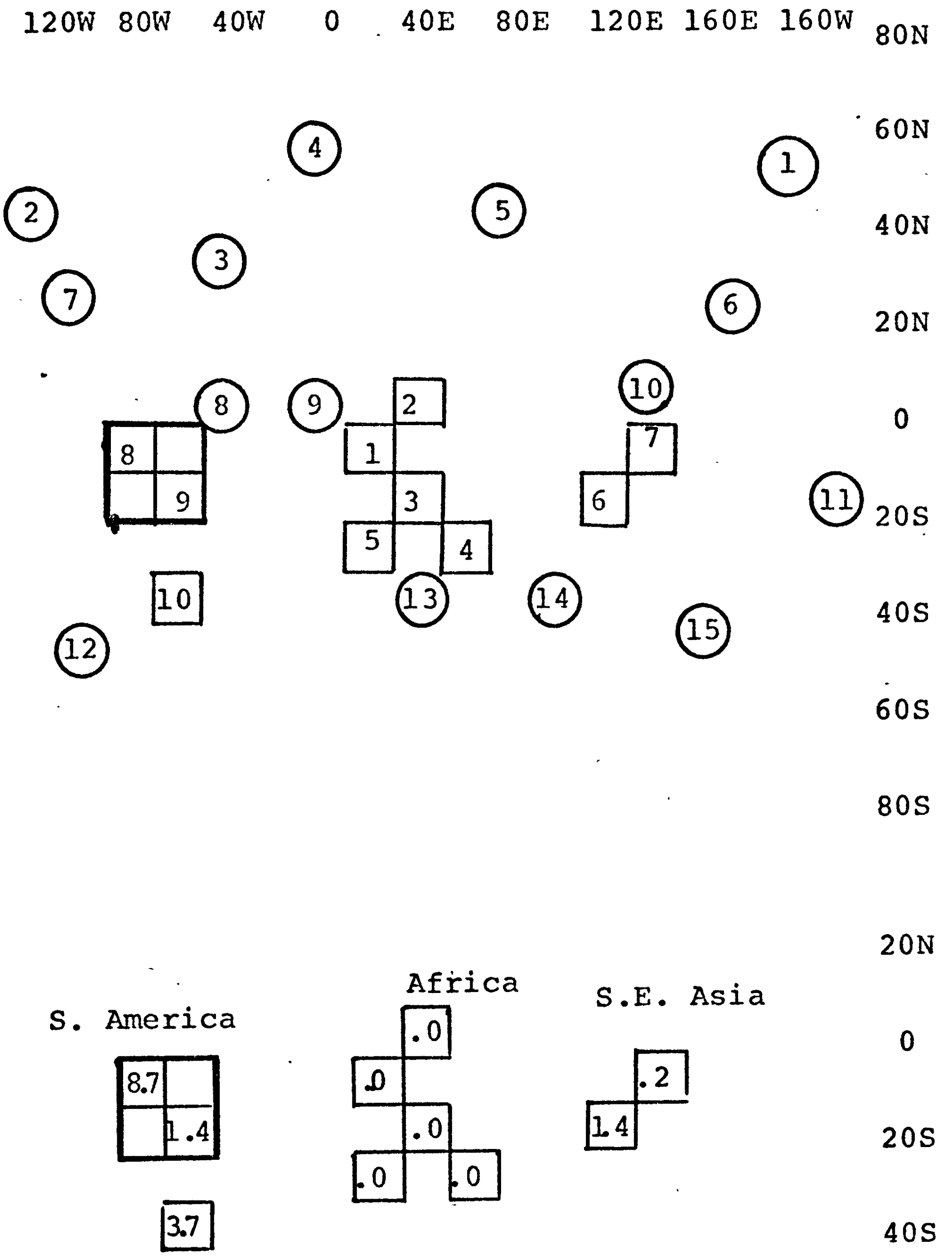

Fig. 6-1. Schematic of received power inversion numerical experiment. In the upper figure the encircled numbers represent stations, and the squares represent possible source locations. The 40 x 20 box enclosing source locations 8 and 9 and the lower graph are concerned with the inversion trial described in the text.

energy appears erroneously in the Southeast Asia locations; this is the antipodal effect discussed above. Since the solution zones do not completely overlap the actual source zones, some of the source energy spills into a solution zone to the south.

Since a network of world-wide receiving stations will be able to furnish a good deal of subsidiary information about thunderstorm location, the source problem appears quite tractable when treated in this manner.

6.3 Location of Ionospheric Pertubations - Technique

Although locating storm sources using observed amplitude data is fairly straightforward, the application of frequency and Q observations in dealing with the nature of ionospheric changes is more involved. We must know the characteristics of what we might loosely term an "unperturbed" ionosphere and also the thunderstorm locations before beginning to acquire knowledge of the perturbations from peak frequency and Q changes. As is usual in geophysical interpretation problems, we might wish to compile a small catalog of effects produced by ionization changes using different combinations of areal extents, vertical distributions, and intensities, similar to the examples of Chapter 3. If only a handful of stations were available, this would probably be the better approach. However, presupposing data from a dozen or so stations, a direct inversion scheme appears feasible and this approach is examined in what follows.

The observed frequency and Q changes will be caused by a mix of the changes in damping and propagation of the waves in the perturbed regions of the ionosphere. Dividing the earth into sectors (see fig. 6-2) to serve as possible locations for perturbing influences and adopting the phase velocity v and quality factor q characterize the perturbations, we set up the formulation:

$$\Delta Q_i = \frac{\Delta Q_i}{\Delta q_i} \Delta q_j + \frac{\Delta Q_i}{\Delta v_j} \Delta v_j \tag{6-2}$$

$$\Delta F_i = \frac{\Delta F_i}{\Delta q_j} \Delta q_j + \frac{\Delta F_i}{\Delta v_j} \Delta v_j$$

where

Q_i is the Q change observed at station "i"

F_i is the peak frequency changes observed at staion "i"

q_j is the Q change in the sector "j"

v_j is the phase velocity change in sector "j"

$i=1,\ldots,i_o$ where i_o is the number of stations

$j=1,\ldots,j_o$ where j_o is the number of sectors

In the examples which follow $i_o=12$ and $j_o=8$, so the least-square formulation of equations 6-2 leads to a 16 x 16 matrix inversion problem. However, assessment of the various terms at a mid-latitude station in the southern hemisphere for perturbation effects covering the day temperate zone in the northern hemisphere are:

$$\Delta Q = .17 \text{ (due to } \Delta q = q_o) + .06 \text{ (due to } \Delta v = 0.1c)$$

$$\Delta F = .01 \text{ (due to } \Delta q = q_o) + .14 \text{ (due to } \Delta v = 0.1c)$$

The remarks in parentheses indicte that the q's were doubled and the phase velocities changed by 0.1 of the speed of light to obtain the numbers cited. Thus, while a change in phase velocity influences both observed Q and peak frequency, altering the q of the sector produces an effect on the peak frequency less than 10% of the Δv_j effect. Since this example is representative, we will deal with the problem of determining Δv_j directly from the ΔF_j terms. It appears possible to work further and, after eliminating the contributions of Δv_j on ΔQ_i, to use the remaining ΔQ_i information to solve for Δq_j, but this is not examined here.

6.4 Location of Ionospheric Perturbations - Numerical Example

Figure 6-2a displays the frequency changes "observed" at 12 sites due to phase velocity changes in the propagation characteristics over the polar caps. If Q changes had been included, this model would simulate a PCA event. The computed frequency shifts, ΔF, range from -.174 to -.253 cps at the 12 stations. The eight sectors of the figure reprsent the division of the earth into 2 polar cap

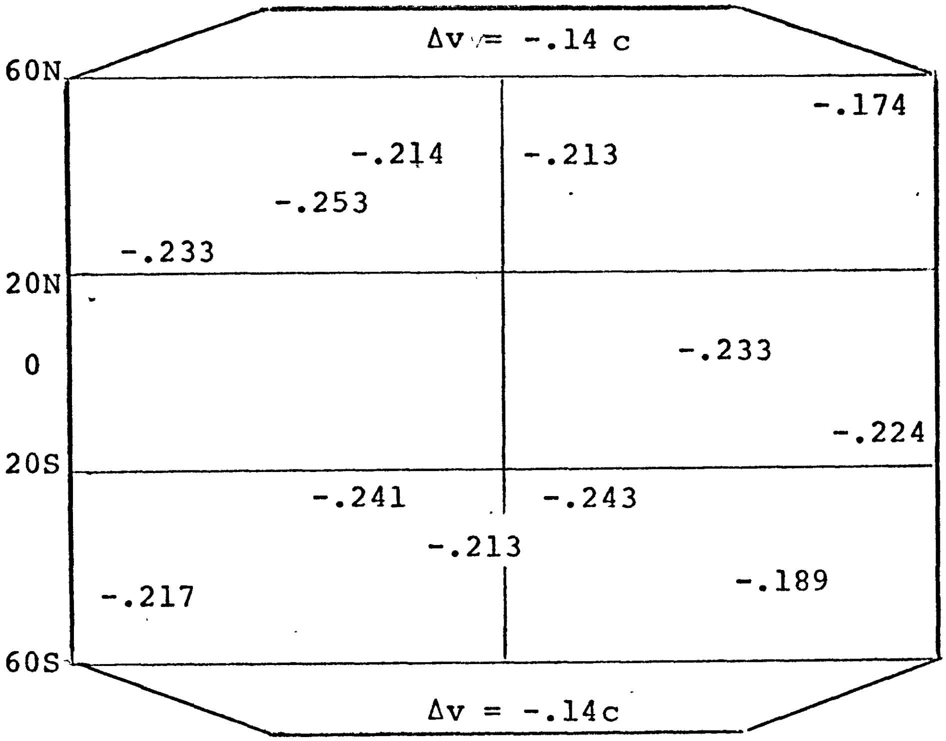

Fig. 6-2a. Frequency changes (Δf) at 12 stations due to phase velocity decreases (Δv = -.14c) over polar caps.

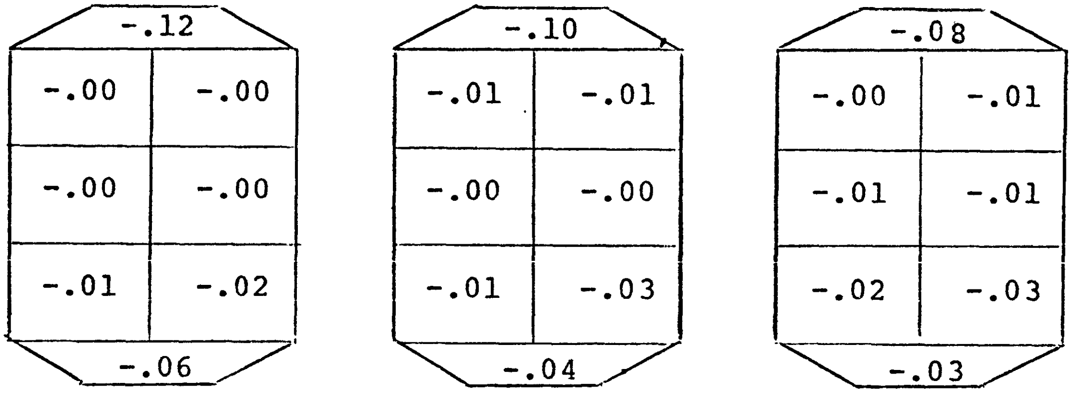

accurate data
3.5% residual

data with 5% errors
5.0% residual

10% errors
10% residual

Fig. 6-2b. Solutions for Δv using inversion scheme with no errors, 5%, and 10% errors in ΔF. The ΔF data is given in Fig. 6-2a.

sectors, 1 day equatorial sector, 1 night equatorial sector, 2 day temperate zone sectors and 2 night temperate zone sectors. These various sectors serve as possible locations for a perturbation, in this case Δv, as described in the previous section.

The iterative technique used to invert the "observed" frequency changes is the same as that used for the source inversion. Using the $\Delta F/\Delta v$ coefficients, the ΔF data were used to obtain the Δv results of Fig. 6-2b. The Δv solutions were carried out for no errors, 5% errors and 10% errors in the ΔF information. In the third case, with 10% errors, the ΔF data were restricted to multiples of .05 cps to provide an example within the resolution of the resonance tracker. The residuals indicate the per cent difference between the ΔF input data and the ΔF's which result when the Δv solution is multiplied by the $\Delta F/\Delta v$ coefficient matrix.

The solutions of Fig. 6-2b are fairly good, although the solution for the southern polar sector spills over into the adjacent sectors. An important feature of fig. 6-2b is the stability of the solutions with increasing errors in the data and in the residuals. It appears that with appropriate refinements, such an inversion scheme will be useful in delimiting zones of ionospheric disturbance.

SUMMARY AND CONCLUSIONS

This thesis has dealt firstly, with the construction of an electronic phase-sensitive tracking device for the first Schumann mode, secondly, with an experimental study of the first mode behavior, and thirdly, with the problem of using first resonance mode data to increase our knowledge of ionospheric behavior.

The resonance mode tracker has proven to be capable of monitoring the peak frequency and Q on a continual basis. The tracker is stable to within 1% over a period of several months. Because of its simplicity, the tracker represents a considerable saving in both equipment and labor when compared to other experimental techniques.

Results from the tracker show that the first resonance mode is always present, although the observed Q is greatly reduced when the amplitude is low. The reduced Q is probably due to the greater contribution of non-cavity signal when thunderstorm activity is low since the model results predict a fairly uniform Q pattern. It is difficult to assess the non-cavity contribution quantitatively.

The daily amplitude behavior during both summer and winter months follows the patterns predicted by model results in conjunction with world thunderstorm patterns. This substantiates Balser and Wagner's conclusion that thunderstorms are the prime source of cavity excitation.

The diurnal peak frequency behavior displays both a seasonal and a longer-term dependence. During summer months the diurnal peak frequency patterns of individual days are less similar to one another than they are during winter months. This is attributed to the greater time and space variability of North American thunderstorms. During winter months when the predominance of storm activity lies in Africa and South America, the frequency patterns are more regular. The longer-term variations in diurnal behavior show up when data collected over several years are compared. The frequency behavior during 0600-1600 EST underwent several reversals over a period of years. These changes must be accounted for by changes in the thunderstorm patterns; in particular, a shift in the balance between East and West African storms could produce the observed shifts in the frequency pattern.

The daily average peak frequency has undergone an increase from 7.8 cps in 1961 to as high as 8.2 cps in 1967. This kind of long-term change must be due to solar control, but the relationship is not known.

The tracker results show that the cavity is measureably affected by ionospheric changes. Although individual SID events do not consistently produce cavity changes, a sequence of SID events does, and the reduction in peak frequency is consistent with model results. Likewise, the reduction of peak frequency during PCA events is also consistent with models which incorporate ionization increases in the D region.

Magnetic storms produce results unexpected in their nature and strength. The strong increase of Q and some reduction in frequency is typical of isolated magnetic storms. However, when high magnetic activity is sustained for 4 or 5 days the cavity response is not at all clear. Brief studies of ionization changes at different heights suggest that these effects observed during storms are due to world-wide ionization increases in the E region.

There is no doubt that disturbance changes in the ionosphere influence the Schumann resonances and that these influences can be measured. Since the resonance spectrum is always with us, it provides an inexpensive means of continually monitoring both short-term and long-term ionospheric behavior. It is worth emphasizing that the Schumann resonance measurement differs from ionosonde or radio propagation measurements, because rather than sampling ionospheric properties directly overhead or along a propagation path, the resonance measurement samples world-wide ionospheric properties. If monitoring is carried out on a world-wide scale, there appears to be little difficulty in establishing the location of the thunderstorm activity. With this information, the Schumann resonance data can contribute greatly to the improvement of ionospheric models and to the understanding ionospheric perturbations.

SUGGESTIONS FOR FURTHER WORK

Continuation of single station measurements will provide additional data to substantiate the PCA and SID-related effects and hopefully will resolve the problem of long-term solar control upon the average peak frequency.

The relative simplicity of the equipment makes feasible a multi-station observational program. The cavity measurements were unaffected by proximity to the C-4 ionospheric sounder at Millstone Hill, so the ionosonde sites scattered throughout the world are good candidates for resonance monitoring sites. Because of the omni-directional nature of a vertical antenna, it is preferable to record the vertical E field. With the vertical antenna it is a simple step to monitor amplitudes in two additional channels, one higher in the ELF range and another at VLF. Information from these additional channels would help to determine storm locations. They would also record SEA (sudden enhancement of atmospherics) events, providing a more thorough examination of the relationships between SID and cavity behavior.

Continual coordination between the cavity resonance and other types of ionospheric data is of course higly desirable.

At present the effect of ionization density changes as a function of height is only roughly understood. Refined model studies will be of help in interpreting changes which occur in the verical profile during magnetic storms.

APPENDIX A. Resonance Mode tracker Time Constants and Error Analysis

In this appendix we consider the characteristics of the tracking filter loop. Note that we rely on Fig. 4-1 of Chapter 4; the subscripts on voltages refer to the positions indicated by parenthetical letters in Fig. 4-1. (Complete circuit diagrams are given in Appendix B).

A.1 Miller Capacitance as a Tuning Element

The band-pass filter is an RLC filter of low Q, its resonant frequency given by

$$\frac{1}{\omega_0^2} = L\ (C_o + C_m)$$

where L and C_o are fixed values and C_m is a Miller capacitance of value determined by the gain G of amplifier K:

$$C_m = C_1 \cdot (1 - G)$$

This relation comes from considering the current-voltage relation for a capacitor:

$$i = C \frac{dv}{dt}$$

In Fig. 4-1 the voltage v across C_1 is $v_b - G\ v_b$, due to the presence of the amplifier K.

Hence:

$$i = C_1 \frac{d}{dt}\left(v_b - Gv_b\right) = C_1 \ (1-G) \ \frac{dv_b}{dt}$$

and the value of C_1 is modified by the factor 1-G.

A.2 Loop Time Constant

One parameter of interest is the time response of the filter to a step increase in frequency. This time constant is derived by considering the change in phase, ϕ, at point (b). For small phase shifts, the voltage after the gate is

$$v_d = \sin\phi \ E_b \approx \phi E_b \qquad \text{(A-1)}$$

Where E_b is the maximum amplitude of v_b.

The expression for the circuitry between (d) and (e), which we will call a leaky integrator, is

$$R_2C_2 \frac{dv_e}{dt} + v_e = -\frac{R_2}{R_1} v_d$$

We assume that changes in v_e occur in times small compared with R_2C_2, so that

$$R_2C_2 \frac{dv_e}{dt} >> v_e$$

then

$$\frac{dv_e}{dt} = -\frac{R_2}{R_1}\frac{1}{R_2C_2} \quad v_d = + g\frac{E_b}{T_2}\phi \quad \text{(A-2)}$$

where $g = \frac{-R_2}{R_1}$ and $T_2 = R_2C_2$

we relate the voltage v_e and phase ϕ in a linear fashion:

$$k = \phi/v_e = \frac{d\phi}{dv_e}$$

This puts equation (A-2) in the form

$$\frac{d\phi}{dt} \approx \frac{g\ k\ E_b}{T_2}\phi$$

Hence the time constant of the tracker loop is

$$T_t = \frac{T_2}{g\ k\ E_b} \qquad \text{(A-3)}$$

We now determine k, which links the control voltage v_e to the phase ϕ, and which incorporates the gain G of the Miller capacitor and the phase-frequency relation of the LC filter. That is,

$$k = \frac{d\phi}{dv_e} = \frac{d\phi}{d\omega}\frac{d\omega}{dv_e} = \frac{d\phi}{d\omega}\frac{d\omega}{dG}\frac{dG}{dv_e} \qquad \text{(A-4)}$$

The first term, $\frac{d\phi}{d\omega}$, can be determined roughly by considering the two half-power points of the RLC filter where ± 45° phase shift occurs

$$\frac{d\phi}{d\omega} \simeq \frac{\Delta\phi}{\Delta\omega} = \frac{\pi/2}{2\pi\Delta f} = \frac{1}{4}\,\frac{Q}{f}$$

The second derivative $\frac{d\omega}{dG}$ comes from setting the reactance term of the filter transfer function equal to zero:

$$H(\omega) = \frac{Z_L \| Z_C}{R + Z_L \| Z_C} = \frac{\omega L}{\omega L - jR\left[1-\omega^2 L(C_o+C_m)\right]}$$

$$0 = 1 - \omega^2 L(C_o+C_m) = 1 - \omega^2 L(C_o+C_1(1-G))$$

$$G = \frac{C_o+C_1}{C_1} - \frac{1}{\omega^2 LC_1}$$

$$\frac{dG}{d\omega} = \frac{2}{\omega^3 LC_1}$$

Third derivative in the expression for k is $\frac{dG}{dv_e}$ and is built into the design of circuit element K.

We now have

$$k = \pi^3 QLC_1 f^2 \frac{dG}{dv_e}$$

For the actual circuit parameters

$Q = 5$

$f = 8.0$ cps

$$L = 200 \text{ henries}$$

$$C_1 = 0.1\ \mu f$$

$$\frac{dG}{dv_e} = -2$$

we get $$k = 0.40$$

To obtain a suitable T_t we use

$$g = -R_2/R_1 = -1000$$

$$T_2 = R_2C_2 = 200M \times 18\mu = 3600 \text{ secs}$$

$$E_b = .083 \text{ volts}$$

which gives, using eqn. (A-3)

$$T_t = \frac{T_2}{g\ k\ E_b} = 110 \text{ secs}$$

This value checks well with oscillator measurements.

A.3 Steady-State Error and Amplitude Dependence

Suppose an incoming sine wave of frequency f has been the input signal for a time much greater than T_t. Suppose also that f is somewhat greater than the center frequency f_o where the Miller gain is zero. Then the tracker will have settled upon some frequency f'.

This new center frequency f' will not be quite equal to f because some signal will be needed to hold the integrator voltage and maintain the required Miller gain to hold f'. Intuitively, we expect that the size of the frequency error $f_\varepsilon = f - f'$ will depend inversely upon the loop gain. Besides considering a frequency error, we also consider the phase error required to maintian the tracker at the relative phase shift, ϕ'. These phases and frequencies must be related in the following fashion:

$$\phi_\varepsilon/\Delta\phi = f_\varepsilon/\Delta f \tag{A-6}$$

where

$f = f' - f_o \quad f - f_o$ is the frequency shift of the tuned RLC circuit

$\Delta\phi = \phi' - \phi_o$ is the associated phase shift of the tuned circuit

$f_\varepsilon = f - f'$ if the frequency error

$\phi_\varepsilon = \phi - \phi'$ is the associated phase error

f_o and ϕ_o are the resonant frequency and relative phase shift of the filter with no Miller gain.

Even though we are considering a new filter center frequency, the Q will be approximately the same and

$$\Delta\phi = kv_e$$

will still hold. Since we are considering the steady state, the leaky integrator may be considered as a straight amplifier for the D.C. component of v_d, and therefore

$$v_e = gE_b \sin\phi_\varepsilon \simeq gE_b\phi_\varepsilon$$

hence

$$\phi_\varepsilon = \frac{\Delta\phi}{kgE_b}$$

and using (A-6), we get

$$f\varepsilon = \frac{\Delta f}{kE_b g}$$

In our circuitry, kg = 400. If we are operating 1cps off the center frequency ($\Delta f = 1$ cps), then a decrease of E_b from 1.0 to 0.1 volts would cause a 2% change in the frequency estimate while a further decrease from 0.1 to 0.01 volts would cause a 22% change in the estimate.

A.4 Automatic Gain Control

To cure the dependence of the frequency upon the input amplitude, an automatic gain control (AGC) was added to the circuitry (see Figure 4-3). The AGC obtains its input after the signal has passed the filter, so that the peak frequencies most strongly influence the gain control. This ensures that we are controlling the amplitude of the peak energy, and not the amplitude of other regions of the 4.5 - 10.5 cps spectrum.

The time constant in the AGC loop is 5 seconds or about 1/18 T_t so that the amplitude variations are controlled much more quickly than frequency changes. The AGC holds E_b to .083 ± .003 volts over a decade range of input amplitude, so our errors are small.

Appendix B

Resonance Mode Tracker and Filter Schematics

Figures B-1 through B-4 are schematics of the tracking system. Refer to Figure 4-3 for an overall view of the system. Note that the RLC filter and follower appear in each of the first three figures, providing a reference point.

A few comments are in order. Operational amplifiers have been used throughout, thereby saving a great deal of time, since the author had little previous knowledge of the electronics art. Doubtless one could substitute, in places, simpler transistor stages at less expense. The particular amplifiers used depended upon the circuit requirements and upon what was on hand. A high quality amplifier was used in the high impedance leaky integrator circuit; a low quality amplifier serves as a follower. In several places, such as the full-wave rectifiers, a bucking voltage is supplied with a 10K potentiometer and an isolation resistor to counter the effect of offset current from the operational amplifier.

A light-controlled variable resistance device (designated "Raysistor" by the manufacturer) was used as the control device in both the AGC and the frequency control loop.

Since these devices require more current than available from the standard operational amplifier, current boosters were required.

The two clipping circuits which bias the gates employ two 8.2 volt zener diodes in the amplifier feed-back loop. The zener diodes provide very high back resistance and also prevent saturation of the amplifier. Field effect transistors serve as the gates in Figs. B-1 and B-3.

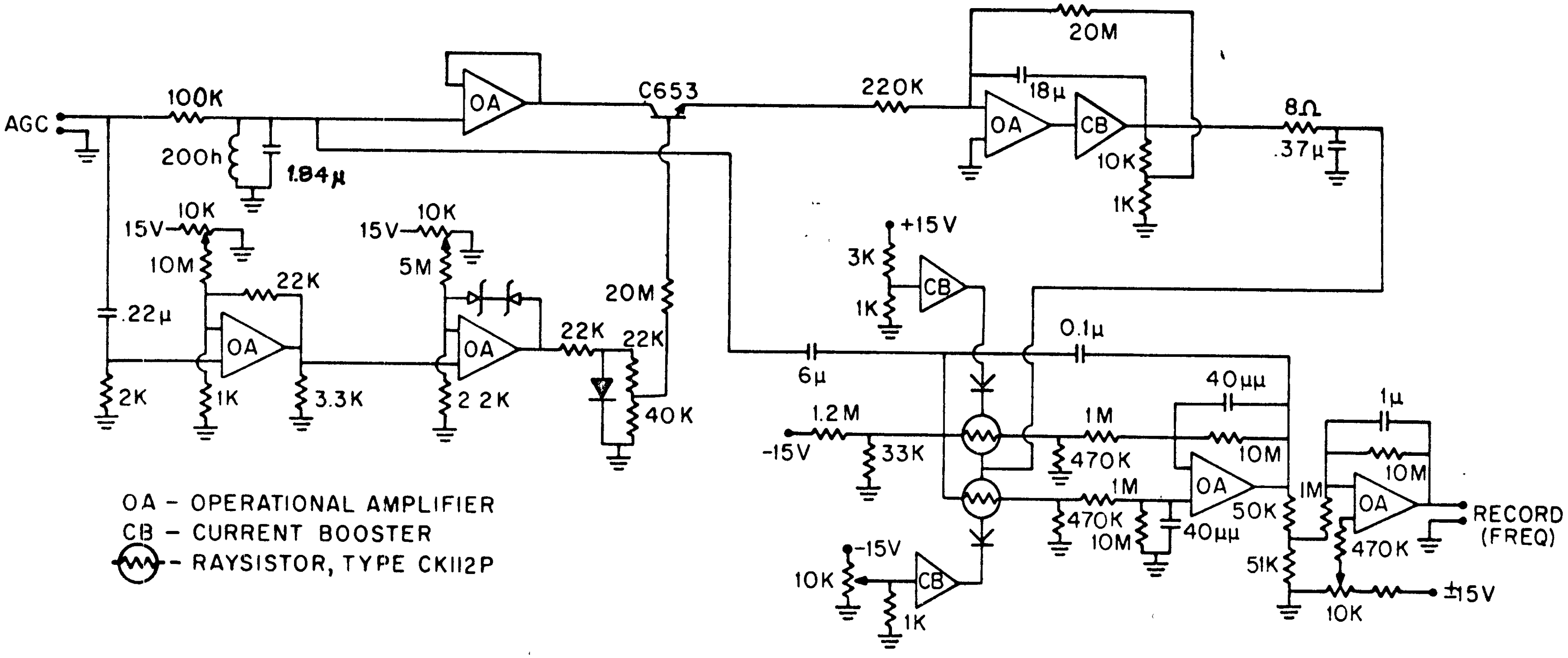

Fig. B-1. Frequency tracking loop schematic, corresponding to elements blocked out in Fig. 4-1.

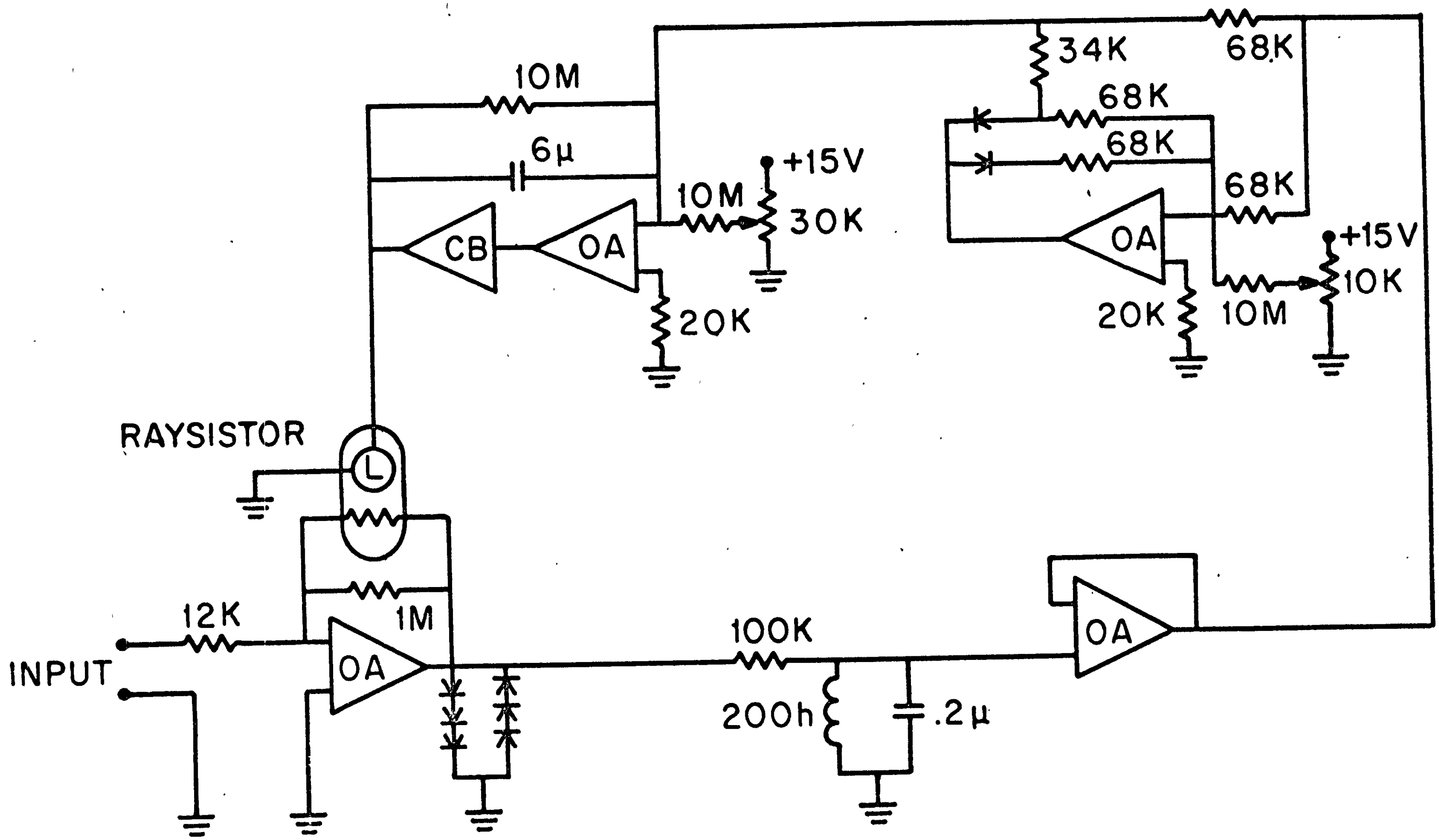

Fig. B-2. Automatic gain control loop and RLC filter.

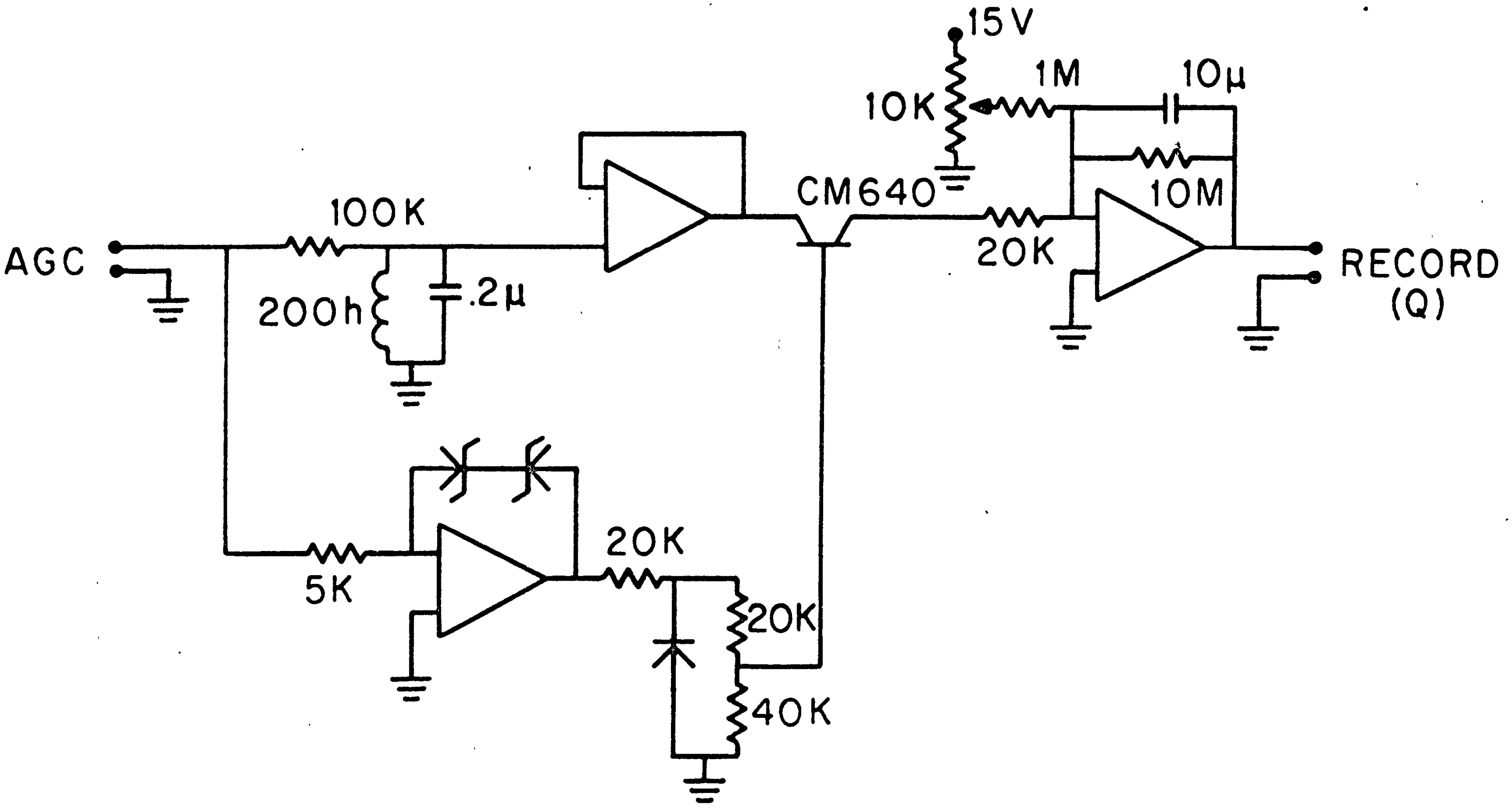

Fig. B-3. Q monitor system: RLC filter, in-phase gate control, gate, and averager.

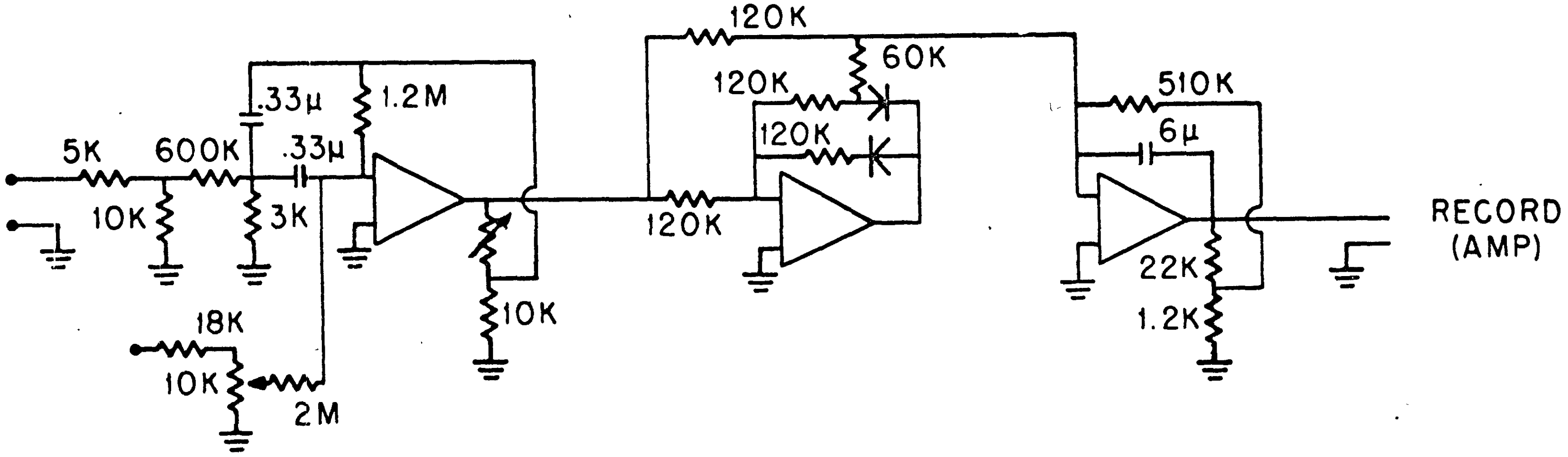

Fig. B-4. Amplitude monitor system: 8.1 cps filter and full-wave rectifier-averager.

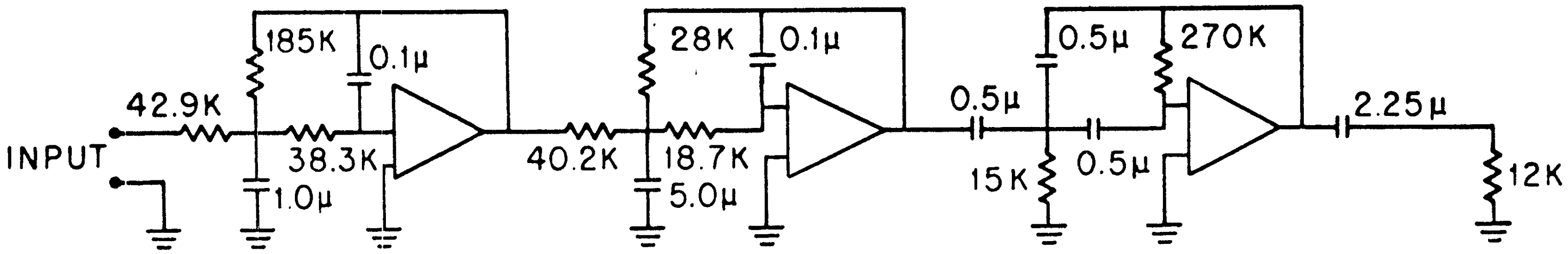

Fig. B-5. 4.5-10.5 cps band-pass filter which precedes the tracker. Filter characteristics given in Fig. B-6.

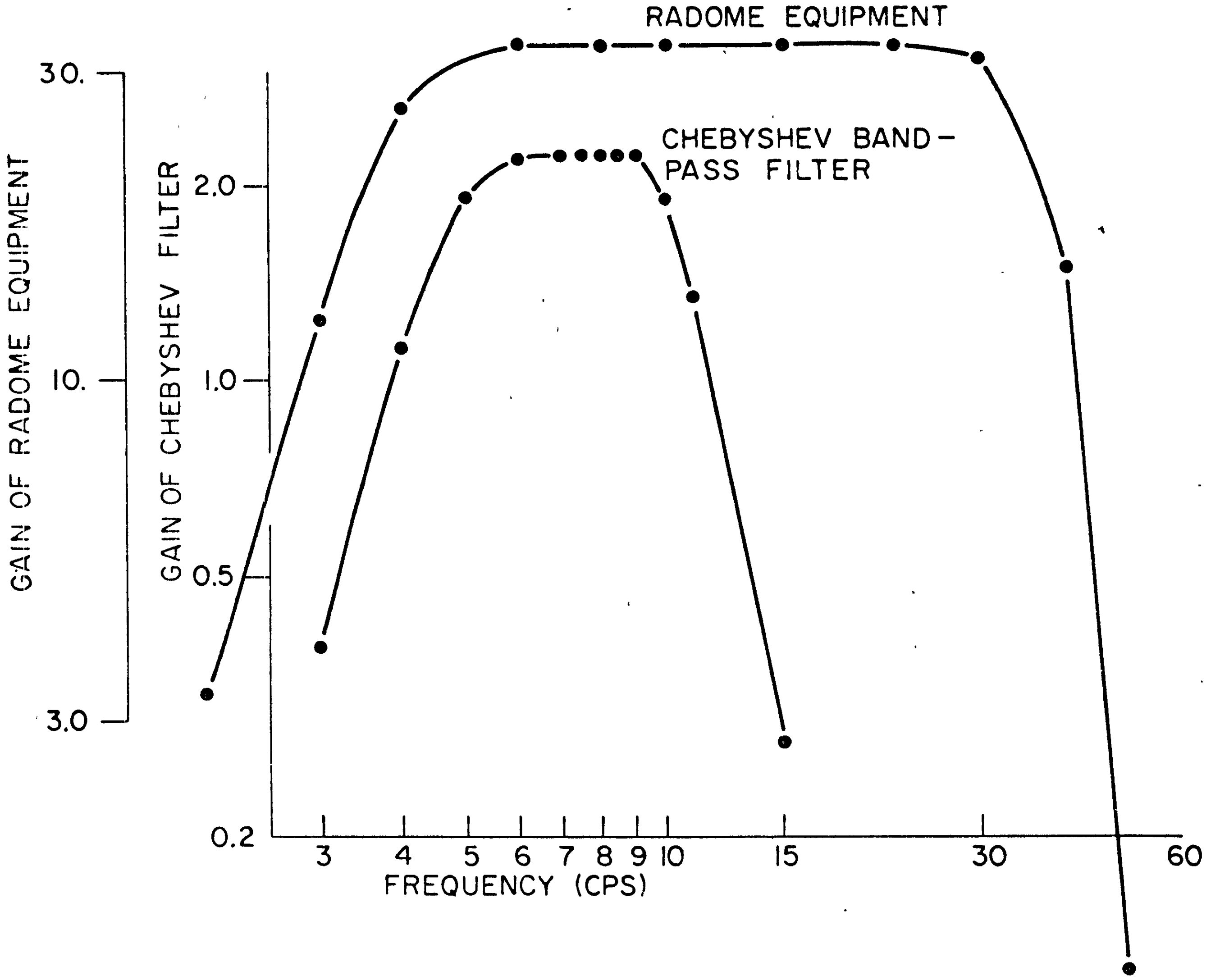

Fig. B-6. Gain characteristics of 4.5-10.5 Chebyshev band-pass filter and radome equipment.

APPENDIX C

Propagation Characteristics for First Mode Model Studies

This appendix contains the propagation characteristics, given as phase velocity and Q, used to obtain the model results described in Chapter 3. The effective cavity height is also given. The parameters represent conditions in tesserae of 20° longitude by 10° latitude. The parameters are averaged at the poles to avoid the computation of artificial derivatives across the polar cap.

The values were taken from Table V of Madden and Thompson.

INPUT DATA - VCC

DAY LOCAL TIME NIGHT

	0720	0840	1000	1120	1240	1400	1520	1640	1800	1920	2040	2200	2320	2440	0200	0320	0440	
80°	.734	.734	.734	.734	.734	.734	.734	.734	.734	.734	.734	.734	.734	.734	.734	.734	.734	.734
	.730	.730	.730	.730	.730	.730	.730	.730	.730	.751	.751	.751	.751	.751	.751	.751	.751	.751
60°	.736	.736	.736	.736	.736	.736	.736	.736	.736	.755	.755	.755	.755	.755	.755	.755	.755	.755
	.740	.740	.740	.740	.740	.740	.740	.740	.740	.760	.760	.760	.760	.760	.760	.760	.760	.760
40°	.745	.745	.745	.745	.745	.745	.745	.745	.745	.764	.764	.764	.764	.764	.764	.764	.764	.764
	.752	.752	.752	.752	.752	.752	.752	.752	.752	.764	.764	.764	.764	.764	.764	.764	.764	.764
20°	.760	.760	.760	.760	.760	.760	.760	.760	.760	.764	.764	.764	.764	.764	.764	.764	.764	.764
	.768	.768	.768	.768	.768	.768	.768	.768	.768	.764	.764	.764	.764	.764	.764	.764	.764	.764
0°	.776	.776	.776	.776	.776	.776	.776	.776	.776	.770	.770	.770	.770	.770	.770	.770	.770	.770
	.776	.776	.776	.776	.776	.776	.776	.776	.776	.770	.770	.770	.770	.770	.770	.770	.770	.770
20°	.768	.768	.768	.768	.768	.768	.768	.768	.768	.764	.764	.764	.764	.764	.764	.764	.764	.764
	.760	.760	.760	.760	.760	.760	.760	.760	.760	.764	.764	.764	.764	.764	.764	.764	.764	.764
40°	.752	.752	.752	.752	.752	.752	.752	.752	.752	.764	.764	.764	.764	.764	.764	.764	.764	.764
	.745	.745	.745	.745	.745	.745	.745	.745	.745	.764	.764	.764	.764	.764	.764	.764	.764	.764
60°	.740	.740	.740	.740	.740	.740	.740	.740	.740	.760	.760	.760	.760	.760	.760	.760	.760	.760
	.736	.736	.736	.736	.736	.736	.736	.736	.736	.755	.755	.755	.755	.755	.755	.755	.755	.755
80°	.730	.730	.730	.730	.730	.730	.730	.730	.730	.751	.751	.751	.751	.751	.751	.751	.751	.751
	.734	.734	.734	.734	.734	.734	.734	.734	.734	.734	.734	.734	.734	.734	.734	.734	.734	.734

Table C-1. Phase velocity divided by speed of light.

INPUT DATA - Q

DAY — LOCAL TIME — NIGHT

	0720	0840	1000	1120	1240	1400	1520	1640	1800	1920	2040	2200	2320	2440	0200	0320	0440
80°	3.400	3.400	3.400	3.400	3.400	3.400	3.400	3.400	3.400	3.400	3.400	3.400	3.400	3.400	3.400	3.400	3.400	3.400
	5.200	5.200	5.200	5.200	5.200	5.200	5.200	5.200	5.200	1.900	1.900	1.900	1.900	1.900	1.900	1.900	1.900	1.900
60°	5.500	5.500	5.500	5.500	5.500	5.500	5.500	5.500	5.500	2.100	2.100	2.100	2.100	2.100	2.100	2.100	2.100	2.100
	5.700	5.700	5.700	5.700	5.700	5.700	5.700	5.700	5.700	2.500	2.500	2.500	2.500	2.500	2.500	2.500	2.500	2.500
40°	6.000	6.000	6.000	6.000	6.000	6.000	6.000	6.000	6.000	2.800	2.800	2.800	2.800	2.800	2.800	2.800	2.800	2.800
	6.200	6.200	6.200	6.200	6.200	6.200	6.200	6.200	6.200	3.200	3.200	3.200	3.200	3.200	3.200	3.200	3.200	3.200
20°	6.400	6.400	6.400	6.400	6.400	6.400	6.400	6.400	6.400	3.400	3.400	3.400	3.400	3.400	3.400	3.400	3.400	3.400
	6.700	6.700	6.700	6.700	6.700	6.700	6.700	6.700	6.700	3.800	3.800	3.800	3.800	3.800	3.800	3.800	3.800	3.800
0°	6.900	6.900	6.900	6.900	6.900	6.900	6.900	6.900	6.900	4.900	4.900	4.900	4.900	4.900	4.900	4.900	4.900	4.900
	6.900	6.900	6.900	6.900	6.900	6.900	6.900	6.900	6.900	4.900	4.900	4.900	4.900	4.900	4.900	4.900	4.900	4.900
20°	6.700	6.700	6.700	6.700	6.700	6.700	6.700	6.700	6.700	3.800	3.800	3.800	3.800	3.800	3.800	3.800	3.800	3.800
	6.400	6.400	6.400	6.400	6.400	6.400	6.400	6.400	6.400	3.400	3.400	3.400	3.400	3.400	3.400	3.400	3.400	3.400
40°	6.200	6.200	6.200	6.200	6.200	6.200	6.200	6.200	6.200	3.200	3.200	3.200	3.200	3.200	3.200	3.200	3.200	3.200
	6.000	6.000	6.000	6.000	6.000	6.000	6.000	6.000	6.000	2.800	2.800	2.800	2.800	2.800	2.800	2.800	2.800	2.800
60°	5.700	5.700	5.700	5.700	5.700	5.700	5.700	5.700	5.700	2.500	2.500	2.500	2.500	2.500	2.500	2.500	2.500	2.500
	5.500	5.500	5.500	5.500	5.500	5.500	5.500	5.500	5.500	2.100	2.100	2.100	2.100	2.100	2.100	2.100	2.100	2.100
80°	5.200	5.200	5.200	5.200	5.200	5.200	5.200	5.200	5.200	1.900	1.900	1.900	1.900	1.900	1.900	1.900	1.900	1.900
	3.400	3.400	3.400	3.400	3.400	3.400	3.400	3.400	3.400	3.400	3.400	3.400	3.400	3.400	3.400	3.400	3.400	3.400

Table C-2. Q values.

INPUT DATA - ALT

				DAY					LOCAL TIME					NIGHT				
	0720	0840	1000	1120	1240	1400	1520	1640	1800	1920	2040	2200	2320	2440	0200	0320	0440	
80°	54000	54000	54000	54000	54000	54000	54000	54000	54000	54000	54000	54000	54000	54000	54000	54000	54000	54000
	52000	52000	52000	52000	52000	52000	52000	52000	52000	56000	56000	56000	56000	56000	56000	56000	56000	56000
60°	52000	52000	52000	52000	52000	52000	52000	52000	52000	56000	56000	56000	56000	56000	56000	56000	56000	56000
	52000	52000	52000	52000	52000	52000	52000	52000	52000	56000	56000	56000	56000	56000	56000	56000	56000	56000
40°	52000	52000	52000	52000	52000	52000	52000	52000	52000	56000	56000	56000	56000	56000	56000	56000	56000	56000
	52000	52000	52000	52000	52000	52000	52000	52000	52000	56000	56000	56000	56000	56000	56000	56000	56000	56000
20°	52000	52000	52000	52000	52000	52000	52000	52000	52000	56000	56000	56000	56000	56000	56000	56000	56000	56000
	52000	52000	52000	52000	52000	52000	52000	52000	52000	56000	56000	56000	56000	56000	56000	56000	56000	56000
0°	52000	52000	52000	52000	52000	52000	52000	52000	52000	56000	56000	56000	56000	56000	56000	56000	56000	56000
	52000	52000	52000	52000	52000	52000	52000	52000	52000	56000	56000	56000	56000	56000	56000	56000	56000	56000
20°	52000	52000	52000	52000	52000	52000	52000	52000	52000	56000	56000	56000	56000	56000	56000	56000	56000	56000
	52000	52000	52000	52000	52000	52000	52000	52000	52000	56000	56000	56000	56000	56000	56000	56000	56000	56000
40°	52000	52000	52000	52000	52000	52000	52000	52000	52000	56000	56000	56000	56000	56000	56000	56000	56000	56000
	52000	52000	52000	52000	52000	52000	52000	52000	52000	56000	56000	56000	56000	56000	56000	56000	56000	56000
60°	52000	52000	52000	52000	52000	52000	52000	52000	52000	56000	56000	56000	56000	56000	56000	56000	56000	56000
	52000	52000	52000	52000	52000	52000	52000	52000	52000	56000	56000	56000	56000	56000	56000	56000	56000	56000
80°	52000	52000	52000	52000	52000	52000	52000	52000	52000	56000	56000	56000	56000	56000	56000	56000	56000	56000
	54000	54000	54000	54000	54000	54000	54000	54000	54000	54000	54000	54000	54000	54000	54000	54000	54000	54000

Table C-3. Effective height of cavity in meters.

APPENDIX D

Evaluation of the First-Order Perturbation Technique

The first-order perturbation technique is tested by perturbing one homogeneous model so that the result is a second homogeneous model and comparing this solution with the analytic solution.

The test involves three solutions, analytic solution for homogeneous model (a) and for homogeneous model (c), and a perturbation solution for model (a), perturbed to model (c). Figure D-1 illustrates the evaluation results. All three models had completely uniform Q's (Q=6.0), effective heights (52 km.), and phase velocities. In model (a) the phase velocities equal .745 c everywhere and the peak frequencies form V_a^o are plotted (the V_a' solution is of course the same as V_a^o, since the perturbation is zero). Model (b) uses the eigenvalues (designated λ in the figure) of model (a) so that V_b^o and V_a^o are identical. However the phase velocities of model (b) are .685 c everywhere, introducing inhomogeneous secondary source terms. The result is the V_b' solution which is perturbed toward the results of the homogeneous model (c). The phase velocities of model (c) are also .685 c everywhere, so if our solution scheme were perfect, the peak frequency results of V_b' would be identical to those of V_c^o.

The error of the V' solution is about 20% of the correct V^{o} solution over the major portion of what is examined here. The 0.4 cps difference between models (a) and (c) is twice as great as that needed for most ionospheric perturbation events.

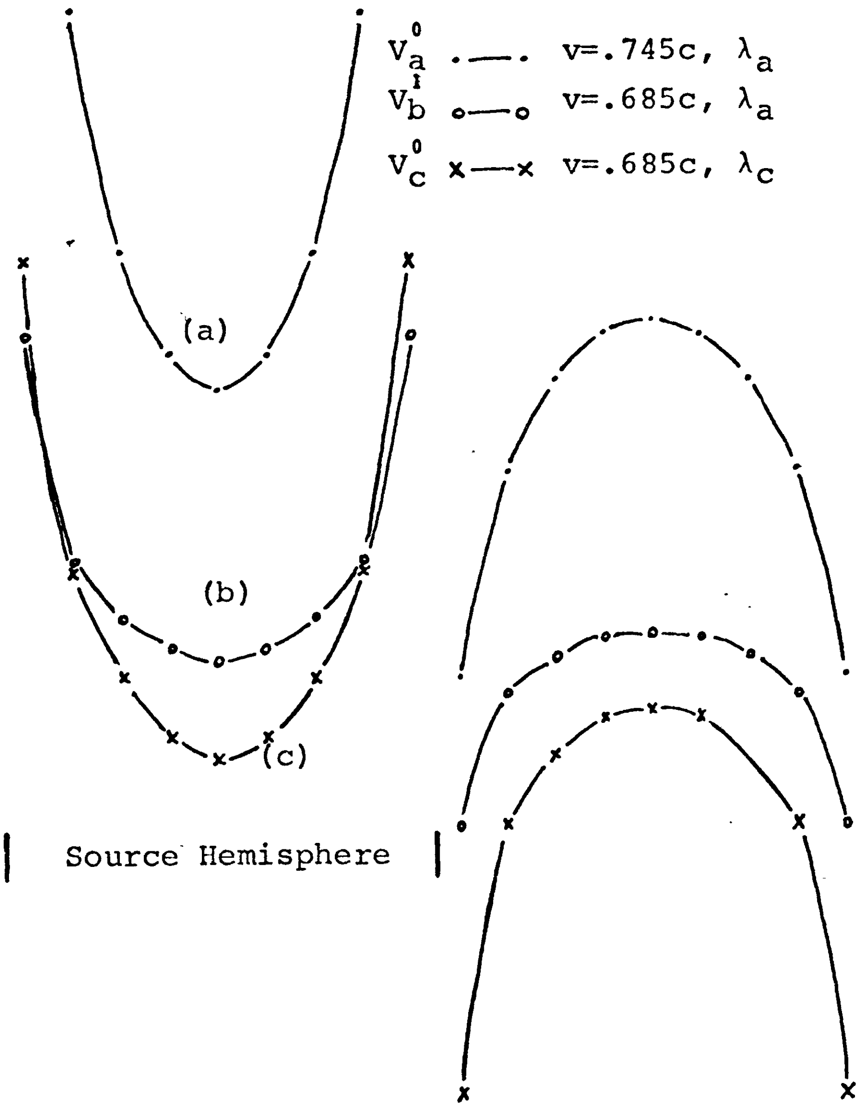

Fig. D-1. Peak frequencies along 45° latitude with the source on the equator. The three models deal with the test of the first-order perturbation technique, as described in the text. The propagation parameters of model (a) are representative of daytime conditions with mid-latitude magnetic field, as given by Madden and Thompson.

BIBLIOGRAPHY

Balser, M., and C. Wagner, Diurnal Power Variations of the Earth-Ionosphere Cavity Modes and Their Relationship to World-Wide Thunderstorm Activity, J.G.R., 67, 619-625, 1962.

Balser, M., and C. Wagner, On Frequency Variations of the Earth-Ionosphere Cavity Modes, J.G.R., 67, 4081-4083, 1962.

Balser, M., and C. Wagner, Effect of a High-Altitude Nuclear Detonation on the Earth-Ionosphere Cavity, J.G.R., 68, 4115-4118, 1963.

Balser, M., and C. Wagner, "Earth Resonance" in Propagation of Radio Waves at Frequencies below 300 Kilocycles, AGARDograph 74, MacMillan Co., N.Y., 1964.

Blackband, W.T. (ed.), Propagation of Radio Waves at Frequencies Below 300 KC/S. AGARDograph 74, MacMillan Co., N.Y., 1964.

Gardner, F.M., Phaselock Techniques, John Wiley and Sons, Inc., 1966.

Grendrin, R., and R. Stefant, Magnetic Records Between 0.2 - 30 c/s in Propagation of Radio Waves at Frequencies Below 300 Kilocycles, AGARDograph 74, MacMillan Co., N.Y., 1964.

Handbook of Geophysics, Air Force Research Division, Geophysics Research Directorate, MacMillan Co., N.Y., 1960.

Jackson, J.D., Classical Electrodynamics, John Wiley & Sons, Inc., New York, 1962.

Madden, T., and W. Thompson, Low Frequency-Electromagnetic Oscillations of the Earth-Ionosphere Cavity, Reviews of Geophysics, 3, 211-254, 1965.

Physics of the Earth's Upper Atmosphere, edited by C.O. Hines, et.al,, Prentice-Hall, Inc., Englewood Cliffs, N.J., 1965.

Preliminary Report and Forecast of Solar-Geophysical Activity, High Altitude Observatory and Space Disturbance Forecast Center, Boulder, Colorado.

Raemer, H.R., On the Spectrum of Terrestrial Radio Noise at Extremely Low Frequencies, J. Res. of NBS, 65 D, 581, 1961.

Rycroft, M.J., Natural Electromagnetic Noise in the Band 2-30 c/s, Resonances of the Earth'Ionosphere Cavity, Ph.D. Thesis, University of Cambridge, 1963.

Wait, J.R., On the Theory of Schumann Resonances in the Earth-Ionosphere Cavity. Can. J. of Physics, 42, 575-582, 1964

BIOGRAPHICAL NOTE

Philip H. Nelson attended high school in Cerro Gordo, Illinois. He received the Bachelor's degree in the Earth Sciences at M.I.T. in 1962, and entered the graduate school the same year.

The author was employed by Geoscience, Inc., during part of his graduate years. Resulting publications include "Deep Resistivity Results from New York and Virginia" with T. Cantwell and J.N. Galbraith, Jr., (J.G.R., Vol. 69) and "Deep Resistivity Measurements in the Pacific Northwest" with T. Cantwell, J. Webb, and A. Orange (J.G.R., Vol. 70).

During the summer of 1966, Mr. Nelson was employed by Exploration Services of the Kennecott Copper Company.